공학석사학위논문

직접수치해석을 이용한 화성 탐사 헬기용 익형 최적 설계 및 로터 공력 성능 분석

Airfoil Optimization and Rotor Aerodynamics Exploration for Mars Helicopter using Direct Numerical Simulation

2025 년 8 월

서울대학교 대학원

항공우주공학과

박 성 중

직접수치해석을 이용한 화성 탐사 헬기용 익형 최적 설계 및 로터 공력 성능 분석

Airfoil Optimization and Rotor Aerodynamics Exploration for Mars Helicopter using Direct Numerical Simulation

지도교수 이 관 중

이 논문을 공학석사 학위논문으로 제출함

2025 년 6 월

서울대학교 대학원

항공우주공학과

박 성 중

박성중의 공학석사 학위논문을 인준함

2025 년 6 월

위 원 장 _____

부위원장 _____

위 원 _____

This master's thesis contains contents of the following conference papers:

[1] S. Park, G. Wilke, Y. Hong, and K. Yee, "Airfoil Optimization and 3D Rotor Aerodynamics Exploration using Mars Helicopter using Direct Numerical Simulation," in *Proc. 51th European Rotorcraft Forum,*, 2025.

[2] S. Park, G. Wilke, Y. Hong, and K. Yee, "Optimization of Low Reynolds Number Airfoil and Numerical Investigation of 3D Rotor Aerodynamics using Direct Numerical Simulation," in *Proc. Korean Society of Computational Fluids Engineering Spring Conference*, 2025

[3] S. Park, G. Wilke, Y. Hong, and K. Yee, "Optimization of Airfoil and 3D Rotor Aerodynamics for Mars Helicopter via Direct Numerical Simulation," in *Proc. Korean Society for Aeronautical and Space Sciences Spring Conference*, 2025.

Thesis Advisory Committee

Kwanjung Yee, Ph. D.	Advisor, Professor Department of Aerospace Engineering, Seoul National University
Kyu Hong Kim, Ph. D.	Chair, Professor Department of Aerospace Engineering, Seoul National University
Donguk Lee, Ph. D.	Committee Member, Associate Professor Department of Unmanned Aircraft Systems, Hanseo University

Abstract

Airfoil Optimization and Rotor Aerodynamics Exploration for Mars Helicopter using Direct Numerical Simulation

Seongjoong Park
Department of Aerospace Engineering
The Graduate School
Seoul National University

This study presents a Direct Numerical Simulation (DNS) based airfoil design optimization and 3D rotor aerodynamic analysis tailored to the challenging low Reynolds number environment of the Martian atmosphere. To enhance the hover performance of the Mars Airborne Explorer (MAE) during Pit craters exploration, airfoils are optimized at three radial stations of the blade to minimize mean drag across a range of design lift coefficients. The optimization employs Improved Geometric Parameterization (IGP) method with Non-Uniform Rational B-Splines (NURBS) and surrogate-based efficient global optimization to efficiently explore the design space. The optimized airfoils demonstrate 21–28% reductions in mean drag compared to the baseline clf5605 airfoil. This improvement is primarily achieved through Sharp Raised-Lip (SRL) and thin-cambered geometries, which force leading-edge shear layer separation and reduce skin-

friction drag. The optimized airfoils are integrated into a full 3D rotor and evaluated under hover conditions. Results show a 7% increase in Figure of Merit and a 7.6% reduction in power coefficient at the design thrust condition. The comparison of 2D and 3D behaviors of the optimized airfoils reveals that the midboard region exhibited similar characteristics in both 2D and 3D, while in the outboard tip region, spanwise flow induces unsteadiness, resulting in behavioral differences. Furthermore, an off-design analysis is carried out to investigate the rotor's performance variations across a broad thrust range.

Keywords: Airfoil Optimization, Mars Helicopter, 3D Rotor Aerodynamics, Low Reynolds Number, Direct Numerical Simulation

Student Number: 2023-28011

Contents

List of Figures

List of Tables

Chapter 1

Introduction

1.1 Motivation and objectives

Mars has consistently been a subject of interest for humanity, especially since the discovery of traces of water. While various countries have conducted Mars exploration missions using orbiters, landers, and rovers, the successful flight of NASA's Ingenuity Mars Helicopter in 2021[6, 7] has drawn significant attention to the development of Mars exploration helicopters. Unlike traditional rovers, Mars helicopters are not constrained by terrain or obstacles, enabling them to explore larger areas at a much faster pace. Therefore, to fully utilize the mobility of the helicopter, it is crucial to select mission target areas with high scientific exploration value.

One such target of interest is Pit craters, which are geological formations that result from the collapse of lava tube ceilings due to past volcanic activity on

Mars. These structures are likely to serve as entrances to massive underground caves, which could have provided protection for organic matter from UV radiation on the Martian surface, making them potential habitats[8]. Consequently, exploring the interior of Pit craters presents a high likelihood of discovering evidence of water or organic material. Due to their vertical crater-like structure, exploration missions within Pit craters primarily involve hovering and axial flight, with hovering accounting for a significant portion of the mission profile. Maximizing rotor hover performance is therefore a critical factor for mission success.

However, the Martian atmosphere presents unique aerodynamic challenges that make direct application of conventional Earth-based rotorcraft design methodologies ineffective. The atmosphere is extremely thin, with an air density of only about 1.6% of Earth's, and is primarily composed of CO_2 (95%), leading to a significantly lower speed of sound (approximately 240 m/s, 70% of Earth's). These conditions result in an operational environment characterized by very low Reynolds numbers ($Re = O(10^3 - 10^4)$) and relatively high local Mach numbers, which severely degrade lift generation and aerodynamic efficiency [9]. At such low Reynolds numbers, viscous effects dominate, producing large-scale flow separations, Laminar Separation Bubble (LSB), and strong sensitivity to geometric features. Additionally, the lower speed of sound amplifies compressibility effects, further complicating aerodynamic design. The airfoils that perform well at moderate or high Reynolds numbers exhibit early

flow separation and substantial performance loss in the Martian flight regime. These challenges highlight the need to investigate airfoil shapes specifically optimized for the low-Reynolds number conditions of the Martian atmosphere, rather than relying on conventional rotorcraft airfoils developed for Earth.

Numerous studies have been conducted to achieve efficient airfoil optimization for Mars atmospheric conditions[10, 11, 2, 12, 13, 14, 15]. Sasaki et al.[10] performed multi-objective optimization for fixed-wing airfoil design in Martian exploration and observed that a sharp leading edge induces flow separation, which subsequently forms a separation bubble that generates a large low-pressure region on the suction side. Koning et al.[11, 2] optimized airfoils for Mars helicopter and confirmed that cambered plate and double-edged plate outperform the clf5605 airfoil used in Ingenuity. Kwon et al.[12] demonstrated that arrow-shaped airfoils induce flow separation, leading to an increased lift-to-drag ratio, and subsequently optimized arrow-shaped airfoils. These studies primarily analyzed airfoil performance using Reynolds-averaged Navier-Stokes (RANS) equation-based Computational Fluid Dynamics (CFD) simulations. However, RANS simulations rely on turbulence models that approximate small-scale turbulent structures, making them insufficient for accurately capturing large-scale flow structures and separation bubble behavior in low Reynolds number environments[16]. To overcome these limitations, Caros et al.[13] conducted airfoil optimization using Direct Numerical Simulation (DNS) to exclude turbulence model influence and incorporate the detailed flow characteristics of

low Reynolds number environments into the design. Since these airfoils were designed based on 2D simulations, it is necessary to verify whether their optimized performance is retained when applied to 3D rotor blades. To address this, Koning et al.[14, 15] analyzed 3D rotors with optimized airfoils using a free wake model-based comprehensive analysis code and observed enhanced rotor performance. However, these studies did not utilize CFD simulations to analyze the performance of 3D rotors incorporating optimized airfoils, nor did they provide a detailed breakdown of the physical mechanisms contributing to airfoil performance improvement under thrust-trimmed condition.

From the findings above, two critical research needs emerge. First, to accurately model the flow characteristics in low Reynolds number conditions, DNS-based rotor CFD simulations are required. Second, a comparative analysis of baseline and optimized airfoils under thrust-trimmed condition is necessary to determine the fundamental physical mechanisms driving the performance improvement of the optimized airfoil.

Therefore, the objectives of this research are threefold: (1) to derive optimized airfoil geometries that can improve the hover performance of the rotor in the Martian environment, (2) to clearly identify the detail physical mechanisms behind the superior performance of the optimized airfoils under thrust-trimmed condition, and (3) to analyze how the performance of the 3D rotor changes when the optimized airfoils are incorporated and to examine how the aerodynamic behavior of the airfoils differs between 2D and 3D environments. Through this

research, the author aims to propose an optimized airfoil design for maximizing the hovering performance of MAE and provide a detailed physical analysis of the factors contributing to performance improvements.

1.2 Contributions of the master's thesis

This master's thesis makes several significant contributions to the aerodynamic design and analysis of Mars exploration rotorcraft, particularly focused on improving hovering performance in the challenging low Reynolds number environment of the Martian atmosphere. The key contributions are summarized as follows:

1. **Derivation of Optimized Airfoils Tailored for Martian Hovering Conditions**

   High-performance airfoils were optimized at three representative radial stations of the Mars Airborne Explorer (MAE) rotor blade. The optimized airfoils achieved 21–28% reductions in mean drag coefficient compared to the baseline clf5605 airfoil, maintaining robust aerodynamic performance across a wide range of lift coefficients relevant to hovering flight. Two distinct geometric features—Sharp Raised-Lip (SRL) and *thin-cambered designs*—were identified as critical for reducing viscous drag and controlling leading edge shear layer separation.

2. **Comprehensive Flow Physics Characterization of Drag Reduction Mechanisms**

   Detailed analyses of pressure distributions, skin friction distributions, and instantaneous vortex structures were conducted to elucidate the aerodynamic mechanisms behind the drag reduction of the optimized airfoils.

The SRL configuration was shown to trigger controlled shear-layer separation, forming a leading-edge laminar separation bubble (LSB) that significantly reduces skin-friction drag at low Reynolds numbers.

3. **Validation and Extension to 3D Rotor-Level Aerodynamics**

   The optimized airfoils were integrated into the full three-dimensional rotor blade of the MAE. 3D DNS simulations were conducted to validate whether the 2D optimized designs maintain performance in realistic rotor environments. The results demonstrated strong agreement between 2D and 3D aerodynamic behaviors for inboard and midboard radial stations. Differences at the blade tip region were identified, primarily caused by spanwise flow and large-scale vortex shedding.

4. **Demonstrated Performance Improvements in Hovering Rotorcraft Applications**

   The optimized rotor exhibited a 7% increase in Figure of Merit (FM) and a 7.6% reduction in power coefficient relative to the baseline Ingenuity rotor at the thrust-trimmed design condition ($C_T/\sigma = 0.125$). Off-design analyses revealed that the optimized rotor consistently outperformed the baseline rotor within the pre-stall operating range, confirming its enhanced aerodynamic efficiency.

1.3 Overview of the master's thesis

The structure of this thesis is organized as follows: Chapter 2 outlines the conceptual design of the Mars Airborne Explorer (MAE). Chapter 3 focuses on the numerical simulation setup, describing the computational domain design, boundary conditions, turbulence models, grid refinement strategy, and validation procedures against experimental or published reference data. This chapter ensures the credibility and robustness of the CFD-based performance predictions used throughout the optimization. Chapter 4 presents the development of the aerodynamic optimization framework. It explains the geometric parameterization strategy for airfoil shape modification and the surrogate-assisted optimization algorithms employed. Chapter 5 describes the optimization task which is derived by design requirements of MAE. Chapter 6 demonstrates the station-wise airfoil optimization process and analyzes the aerodynamic mechanisms responsible for decreased mean drag for the design lift conditions. Chapter 7 extends the optimized airfoils into a full 3D rotor blade design. This chapter evaluates the aerodynamic performance under hover and forward flight conditions using the validated numerical simulation environment, and compares the results with those from the baseline rotor configuration. Finally, Chapter 8 summarizes the major findings of the research, discusses the limitations of the current approach, and proposes future directions.

Chapter 2

Conceptual Design Results of Mars Airborne Explorer

Conceptual design is conducted using Rotorcraft Initial Sizing and Performance Estimation Code and Toolkit III (RISPECT III)[17, 18], a previously developed framework for Mars exploration vertical take-off and landing vehicles. To ensure reliability of the conceptual design, the single rotor configuration of NASA's Ingenuity helicopter[4] is used as a reference. As a result, a 12.3 kg gross weight octocopter is designed to meet the mission requirements of 8 minutes of endurance and a 1 kg payload, while offering enhanced reliability. The conceptual design results are used to derive the design requirements for airfoil optimization to enhance hover performance.

Chapter 3

Numerical Simulation Setups

3.1 Overview of DNS Approach

DNS provides the most physically accurate representation of fluid flows by directly resolving all relevant turbulent scales without any turbulence modeling. Unlike RANS approaches, which rely on closure models and averaged quantities, DNS can explicitly capture unsteady phenomena critical to low Reynolds number aerodynamics—such as LSB, shear-layer instabilities, and vortex shedding. The Martian atmosphere, characterized by a Reynolds number of $Re = O(10^3 - 10^4)$, poses a unique challenge. Viscous forces dominate the flow, and small geometric variations at the airfoil surface can drastically influence aerodynamic performance. The choice of DNS is particularly justified given the importance of capturing transitional flow and unsteady behavior that critically affect drag and lift generation in Martian conditions [13].

3.2 2D Numerical Simulation setup

2D airfoil simulations for optimization are executed using DNS. To address this, DNS simulations are conducted using the FLOWer CFD solver—an extensively validated, block-structured, compressible Navier–Stokes code developed by the German Aerospace Center (DLR) [19]. The inviscid fluxes are computed using the SLAU2 [20] scheme with a 4th-order van Albada limiter which is a reconstruction technique [21], both of which are mildly modified [22]. The turbulence modeling is not employed for DNS. The flow is computed unsteadily using the BDF2OPT scheme [23], where the pseudo-time steps are advanced with the 2nd order Runge-Kutta, accelerated by implicit residual smoothing [24]. The simulation has been carried out for a total of 100 convective time units (CTU, $CTU = c/U_\infty$) with a time step of 1/305 CTU, resulting in 15,250 calculations in total. At each calculation step, the target residual has been set to 10^{-5}.

For the grid, an O-grid type mesh generated by G-cube which is the automatic grid generation tool developed by Wilke, G. [25] has been used. Since the optimization process involves a very large number of simulation cases, it has been necessary to avoid using an excessively large number of grid cells. However, using too few grid cells reduces the reliability of the results. Therefore, a grid convergence study has been carried out on the triangular airfoil, which is also used in the validation section. The simulation conditions have been set to match those of the experiments conducted by Munday et al. [1], specifically

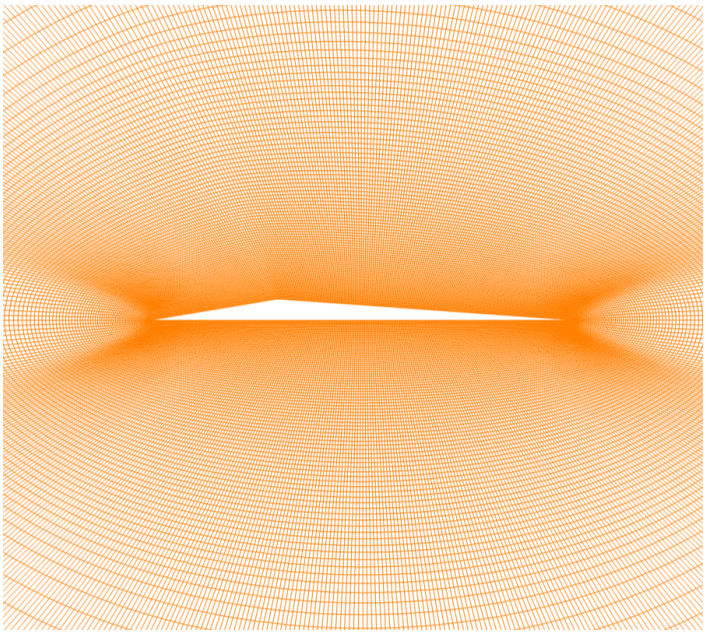

Figure 3.1: Typical grid of triangular airfoil used for simulation.

$M = 0.15,\ Re = 3,000$ and $M = 0.5,\ Re = 3,000$. The generated grids can be seen in Figure 3.1, and the number of grid cells has been increased by a factor of four from the coarsest grid, resulting in four different grid resolutions. The simulations have been performed at $M = 0.15$, $Re = 3,000$ and an angle of attack of 12°, which is predicted to produce unstable flow.

Table 3.1: Grid convergence study results at $M = 0.15$, $Re = 3000$, and $\alpha = 12°$.

Grid size	C_l	ΔC_l [%]	C_d	ΔC_d [%]
Fine (20.6×10^4)	1.249	-	0.2768	-
Medium (7.3×10^4)	1.252	0.253	0.2762	0.196
Coarse (1.8×10^4)	1.238	1.100	0.2756	0.121
Very Coarse (0.5×10^4)	1.185	4.268	0.2610	5.284

The results and the rate of change can be seen in Table 3.1 and Figure 3.2.

It has been confirmed that the differences in lift and drag coefficients between the Medium grid, which has approximately 73,000 cells, and the Fine grid are less than 1%. In addition, simulations for $M = 0.15$ and $M = 0.5$ have been carried out from 0° to 15° angle of attack in 1° increments, and the results are shown in Figure 3.3. At angles of attack below 5°, there has been no difference in lift or drag coefficients among the grids. However, from around 7°, where the flow transitions from steady to unsteady, the results start to show differences depending on the grid. In particular, the Very Coarse grid predicts the angle of attack at which lift increases sharply to be 1° higher. The Coarse grid does not show significant differences compared to finer grids up to 12°, but differences begin to appear beyond 13°. Overall, the results of the Medium and Fine grids have shown differences of less than 1%. Based on this grid convergence study, the Medium resolution grid has been selected as the typical grid for the 2D airfoil simulations, as shown in Figure 3.1. The Medium resolution grid consists of 609 grid points in the chordwise direction and 120 grid points in the normal direction, with a total of approximately 73,000 cells. The near-wall grid spacing has ensured a wall $y+ < 1$, enabling accurate resolution of the viscous sublayer. The far-field boundary has been placed at a distance of 100 chord lengths to prevent reflection of pressure waves.

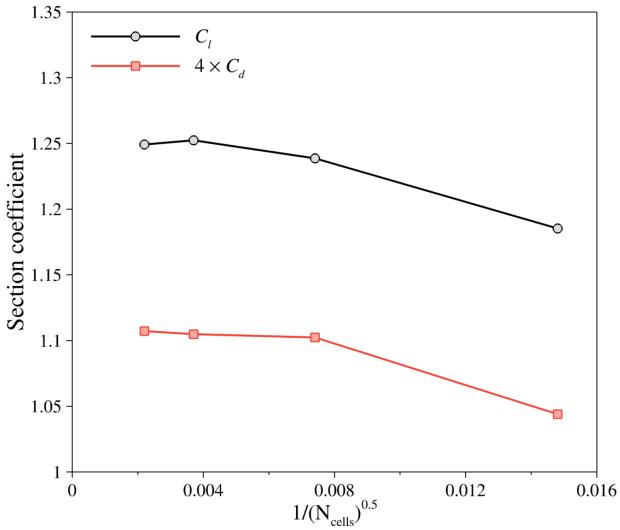

Figure 3.2: Grid convergence study results at $M = 0.15, Re = 3000$, and $\alpha = 12°$.

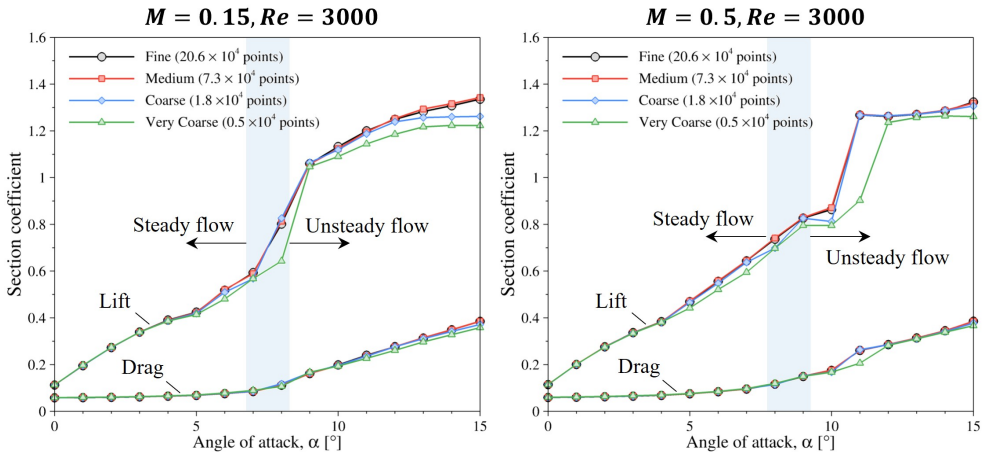

Figure 3.3: Grid convergence study results with lift and drag polars at $Re = 3000$ for $M = 0.15$ and $M = 0.50$.

3.3 3D Numerical Simulation setup

3D rotor simulations for aerodynamic exploration are also carried out using DNS. As with the 2D airfoil simulations, DNS simulations are conducted using the FLOWer CFD solver. The spatial discretization method has been applied in the same way as for the 2D airfoil simulations, and no turbulence model has been used. The integration of physical time and pseudo time has also followed the same procedure as in the 2D simulations; however, for pseudo time, the LU-SGS matrix inversion method has been adopted to ensure solver robustness in the more complex three-dimensional flows. The simulations have been performed for a total of 30 revolutions, applying a quick-start time advancement method. The first 25 revolutions use a time step of 1 degree, and the last 5 revolutions use a finer time step of 0.25 degrees. At each calculation step, the target residual has been set to 10^{-5}.

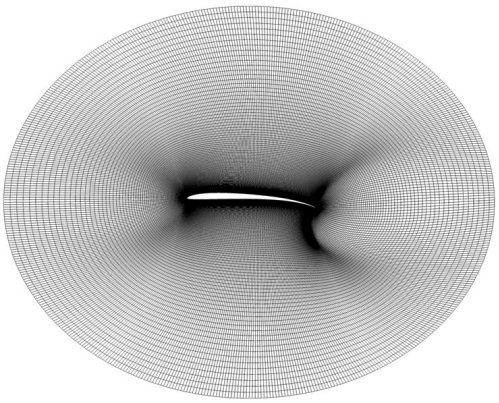

(a) Grid topology of airfoil section

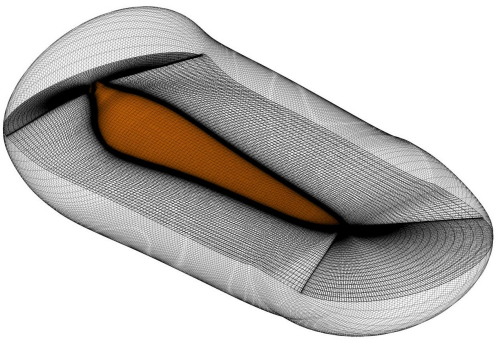

(b) O-O type blade grid

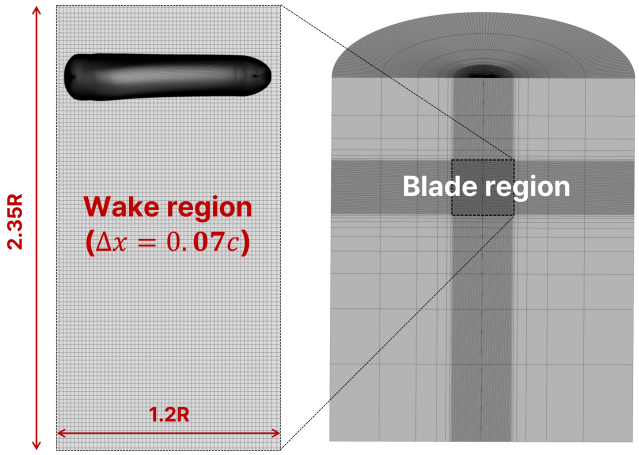

(c) Wake grids and overall background grids

Figure 3.4. Typical grids for 3D rotor aerodynamic simulations.

The grid has been generated using an O-O type mesh produced by G-cube, following the grid generation guidelines of Chaderijan [26] and Koning et al. [5]. All 3D rotor simulations in this study have been carried out under hovering conditions. As with the 2D simulations, a grid convergence study has been conducted for the 3D rotor grids to determine an appropriate grid resolution. The convergence study has been performed on the NASA Transonic Rotor Test (TRT) rotor [5], which is also used later in the validation section. The simulation conditions have been set to match those of NASA's JPL space simulator experiments, specifically the hovering condition with $M_{tip} = 0.75$. The generated grids can be seen in Figure 3.4, and the number of cells has been increased by a factor of eight from the coarsest grid, resulting in three grid resolutions. For the finest grid, which contains an excessively large number of cells, the Richardson method has been used to extrapolate the results instead of directly running the simulation. The results can be found in Table 3.2. It has been confirmed that the differences in thrust coefficient and power coefficient between the Medium grid, which contains approximately 84.5 million total cells (equivalent to 169 million for the full rotor), and the Fine grid are less than 1 percent.

Additional simulations have been conducted at collective pitch angles from 8 to 16 degrees in 2-degree increments, and the results are shown in Figure 3.5. Overall, the Medium and Fine grid results have shown differences of less than 1 percent across all thrust ranges. Based on these grid convergence study results,

Table 3.2: Grid convergence study results for rotor at $M_{tip} = 0.75$.

Grid size	C_T/σ	$\Delta C_T/\sigma$ [%]	C_P/σ	$\Delta C_P/\sigma$ [%]
[a]Fine (676.0×10^6)	0.170	-	0.0275	-
Medium (84.5×10^6)	0.169	0.159	0.0275	0.120
Coarse (10.5×10^6)	0.168	1.110	0.0273	0.678
Very Coarse (1.3×10^6)	0.161	5.097	0.0264	3.824

[a]Coefficients for fine grid are extrapolated using Richardson method

the Medium resolution grid has been selected as the typical grid for 3D rotor simulations, as shown in Figure 3.4. The Medium resolution rotor grid contains 513 cells in the chordwise direction, 129 cells in the normal direction, and 256 cells in the spanwise direction, resulting in a total of 16.9 million cells. The farfield/outer grid contains a total of 67.6 million cells and has been generated as a periodic mesh. Because the target rotor has two blades, the outer grid has been generated as a half-cylinder shape. The near-wall grid spacing has ensured a wall $y+ < 1$, allowing accurate resolution of the viscous sublayer. The wake region of the background grid extends 0.35R above the rotor and 2R below it, with a cell size of 0.07c in the wake region.

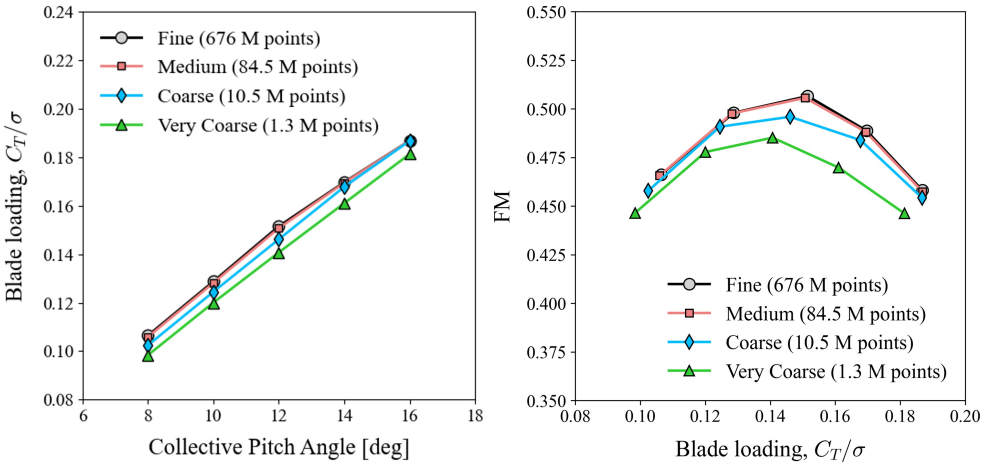

Figure 3.5: Grid convergence study results for rotor at $M_{tip} = 0.75$.

3.4 Validation of Numerical Simulations

3.5 2D Validation results

For validation purposes, the two-dimensional triangular airfoil experimental case conducted by Munday et al. [1] in the Mars wind tunnel is selected. The geometry of the triangular airfoil can be seen in Figure 3.6, and the experimental conditions used in the DNS are summarized in Table 3.3. The 2D DNS simulation results are compared in Figure 3.7 against the experimental lift and drag coefficients measured in the Mars Wind Tunnel [1]. In addition, the Unsteady Navier–Stokes (UNS) simulation results performed by Koning et al. [2] using the OVERFLOW CFD solver and the results from Munday's CharLES DNS are also over-plotted for reference.

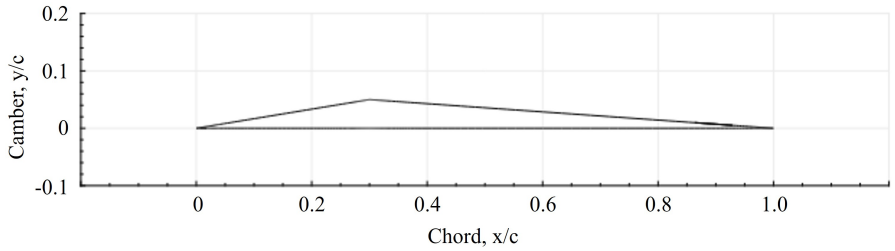

Figure 3.6: Triangular airfoil geometry [1].

Table 3.3: Flow conditions of Mars Wind Tunnel experiment and DNS.

Variable	Mars Wind Tunnel
Reynolds number	3000
Mach number	0.15, 0.5
Specific heat ratio, γ	1.4
Prandtl number	0.71

The FLOWer DNS results obtained in this study show very close agreement with the experimental data at low angles of attack, but a noticeable discrepancy appears in the high angle-of-attack region where the flow transitions to unsteady. This difference is attributed to the fact that the wall effects of the Mars wind tunnel (test section size 10 cm $\times$ 15 cm) have not been modeled in the CFD simulations. The FLOWer results also show similar behavior to Munday's CharLES DNS up to $\alpha = 11°$, but deviate in the higher angle-of-attack region. This difference is likely due to the fact that CharLES has been performed as a 2.5D simulation by extruding the 2D airfoil in the spanwise direction, allowing three-dimensional vortex behavior to be captured. In contrast, the FLOWer DNS results presented here show close agreement with the 2D OVERFLOW UNS results in almost all angles of attack, except at $\alpha = 9°$.

The validation of the pressure coefficient (C_p) distribution has been conducted at angles of attack of 6° and 12°, and the results are shown in Figure 3.8. Each case has been simulated for a total of 50 convective time units (CTU), and the C_p distributions are time-averaged over the final 10 CTU. At $\alpha = 6°$, the FLOWer results show an almost identical distribution to the experimental data and the DNS results from previous studies. In particular, the local suction-side peak at 0.3c is predicted accurately. At $\alpha = 12°$, the FLOWer results show differences compared to the experimental data; however, they show a very similar C_p distribution to the PyFR 2D DNS data, which, like FLOWer, is performed in a purely 2D environment.

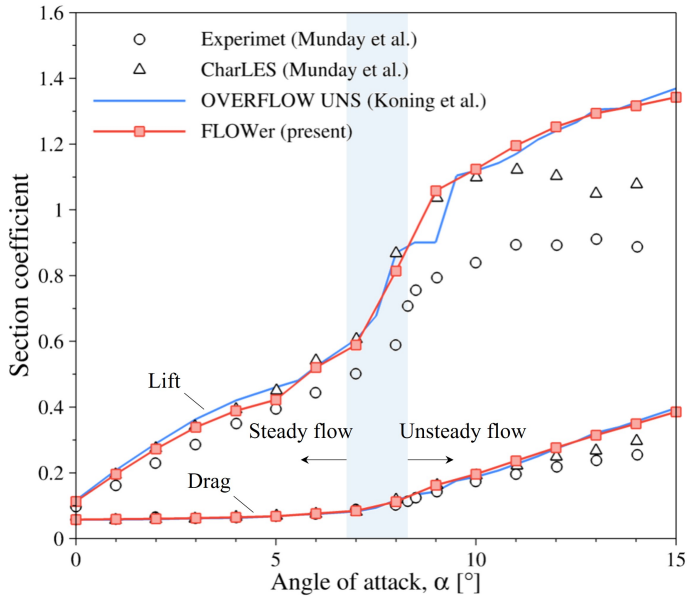

Figure 3.7: Lift and drag coefficient polars compared with experiment results [1] at $M = 0.15$ and $Re = 3,000$.

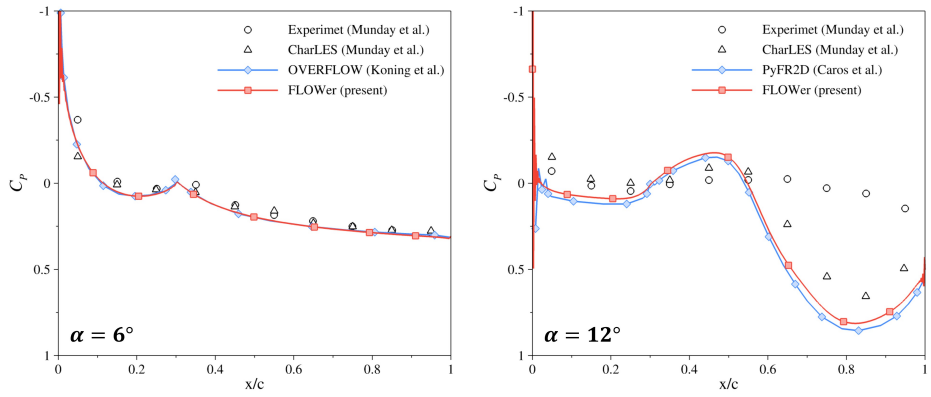

Figure 3.8: Pressure coefficients (C_p) compared with experimental data [1] and CFD data [2, 3] on the suction surface of airfoil (time-averaged).

3.6 3D Validation results

For the three-dimensional validation case, the Transonic Rotor Test (TRT) experiment conducted by NASA in the JPL Space Simulator [5] is selected. The rotor geometry is identical to the single rotor of the coaxial rotor system developed for the NASA/JPL Ingenuity Mars Helicopter. The specifications of rotor is shown in Table 3.4, and the planform information can be found in Koning et al. [5]. The Ingenuity rotor incorporates five different airfoils, with the airfoil distribution along each section. The clf5605 airfoil, which is mainly used in the mid-to-outboard region, is shown in Figure 3.9.

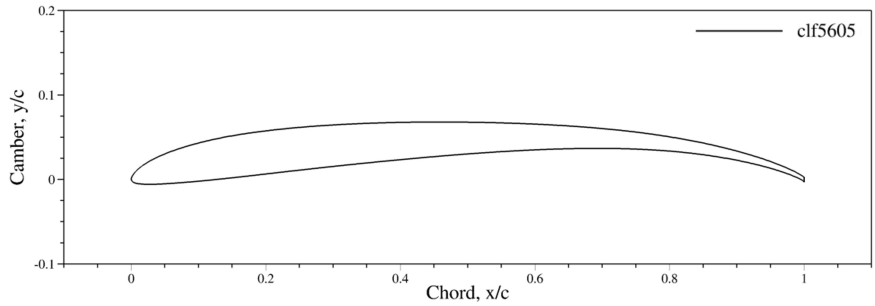

Figure 3.9: clf5605 airfoil geometry of NASA's Ingenuity Mars Helicopter [4]

Table 3.4: Specifications of single rotor from Ingenuity [4]

Parameter	Value
Rotor radius, R [m]	1.225
Disk area, A $[m^2]$	288.2
Blade area $[m^2]$	0.085
Solidity (thrust-weighted), σ	0.07391
Design RPM	2600

The experimental conditions used for the DNS analysis are summarized in

Table 3.5. In the DNS simulations of this study, the OML airfoil geometry, which has a slightly thicker trailing edge for manufacturability, has been applied instead of the designed Ingenuity airfoil to reduce discrepancies with the TRT experimental results. As shown in Figure 3.10, the validation results show less than 10% error between the FLOWer DNS results and the experimental measurements. The difference between the FLOWer results and those obtained using the OVERFLOW is less than 1%.

Table 3.5: Approximate JPLSS test conditions with earth sea-level standard (SLS) conditions.

Variable	Earth (SLS)	TRT
Density, ρ [kg/m^3]	1.225	0.01
Temperature, T [K]	288.2	293.15
Gas constant, R [m^2/s^2/K]	287.1	188.9
Specific heat ratio, γ	1.4	1.289
Dynamic viscosity, μ [N $\cdot$ s/m^2]	$1.75 \cdot 10^{-5}$	$1.46 \cdot 10^{-5}$
Speed of sound, a [m/s]	340.35	267.17

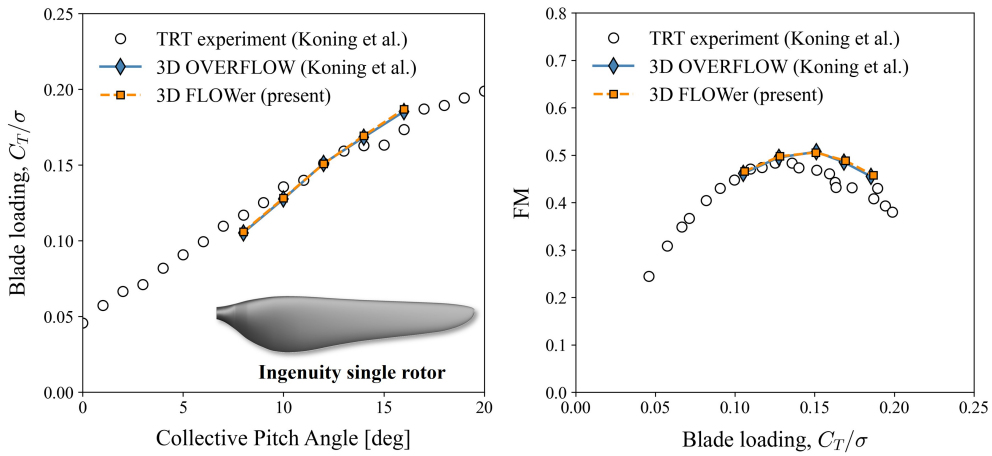

Figure 3.10: Comparison of blade loading C_T/σ versus collective pitch angle (left) and figure of merit (FM) versus blade loading (right) for the Ingenuity single rotor with the experimental data and 3D OVERFLOW simulations [5].

Chapter 4

Optimization Framework

The overarching goal of the optimization framework in this study is to identify airfoil geometries that maximize hovering performance of a MAE under low Reynolds number conditions. Given the dominance of viscous effects and laminar-turbulent transitions in such environments, this work employs a DNS-driven optimization approach, integrated with surrogate modeling and advanced geometric parameterization, to enable physically accurate and computationally feasible design space exploration. The overall optimization framework, POT [27] is illustrated in Figure 4.1. Once a set of design variable combinations capable of defining the airfoil geometry has been generated, the corresponding airfoil shapes are constructed based on these variables. A grid suitable for DNS analysis is then generated using the automated mesh generation tool G-cube [25], and DNS simulations are performed at multiple angles of attack. From the

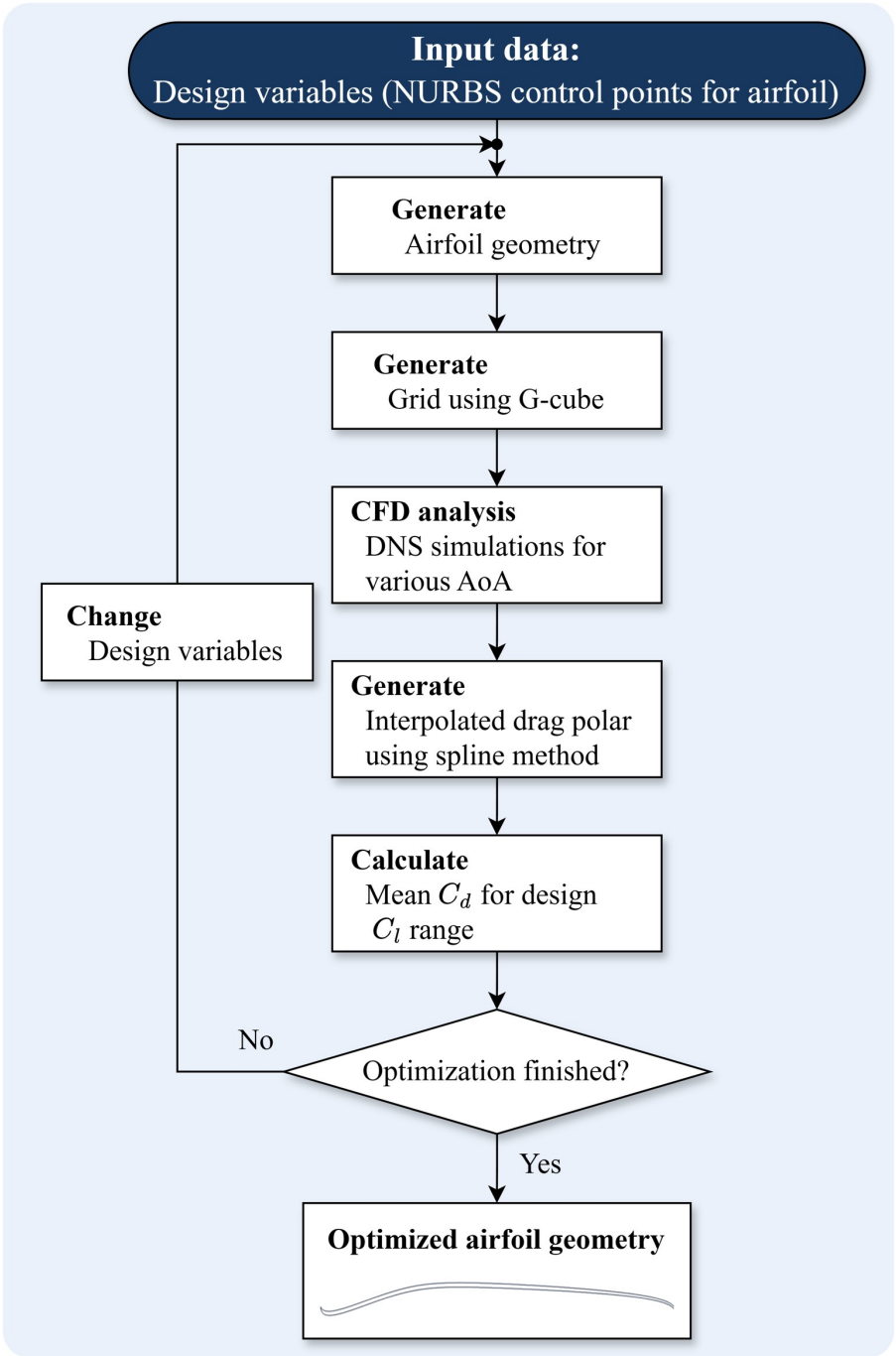

Figure 4.1: DNS-based airfoil optimization framework.

simulation results, the drag polar is reproduced by applying the spline method, allowing the estimation of drag coefficients at angles of attack that have not been directly simulated. Next, the value of the fitness function is calculated. In this study, the fitness function has been defined as the mean drag coefficient ($C_{d_{mean}}$) over a specified range of lift coefficients (C_l). The calculated fitness value is then used to evaluate the convergence criteria of the optimization. If the optimization has not yet converged, a new set of design variable combinations is generated, and the entire framework is repeated from the beginning. Once the optimization process has converged, the final optimized airfoil geometry is obtained.

4.1 Efficient Global Optimziation

To reduce the number of expensive DNS evaluations, a surrogate-based optimization strategy is implemented using the Efficient Global Optimization (EGO) technique [28, 25, 27]. EGO iteratively improves surrogate models by selecting new samples using an acquisition function such as Expected Improvement (EI), balancing exploration and exploitation. The optimization process begins with an initial central Voronoi tessellated (CVT) Latin hypercube [29] of 150 design points to broadly explore the design space. Based on these initial samples, a Kriging model [30] is constructed as the surrogate response surface. Subsequently, the surrogate model is adaptively refined through 8 iterations, during which four new sampling points are selected to find the optimum points and progressively enhance the model's accuracy. For each improvement cycle of refining surrogate modeling and final optimization, Differential Evolution (DE) algorithm combined with a Hooke and Jeeves pattern search method are employed as optimizer to ensure both global and local convergence. The DE algorithm explores the design space efficiently by utilizing vector differences between randomly selected individuals to generate trial solutions. This population-based approach maintains diversity and prevents premature convergence, which is particularly important for high-dimensional design problems. Once promising regions in the design space are identified, the Hooke and Jeeves local search is applied near the current best solution to refine the optimum with higher precision. This hybrid strategy takes advantage of the global search ca-

pability of DE and the fine-tuning capability of the pattern search method, enabling the optimizer to balance exploration and exploitation effectively.

4.2 Parameterization Method

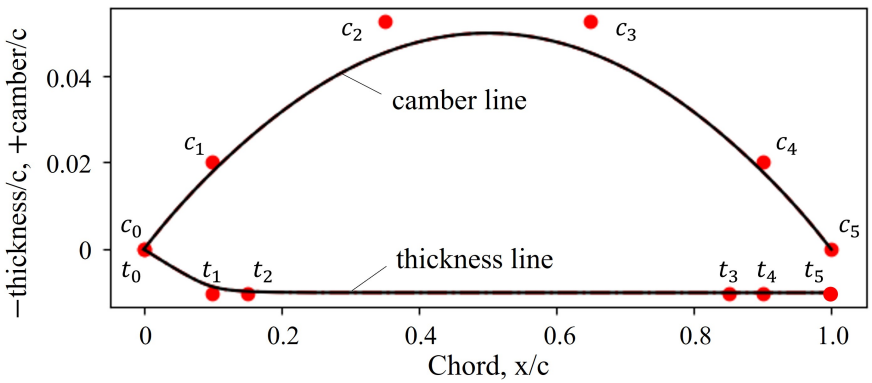

Figure 4.2: Definition of NURBS for decoupled camber and thickness.

Geometric Parameterization (IGP) method based on Non-Uniform Rational B-spline (NURBS) is adopted [31, 27]. This method enables independent control of the camber line and thickness distribution, allowing a broad range of geometries to be expressed without introducing discontinuities. The camber line is expressed by NURBS using six control points, (x_i, y_i), denoted as $c_i(x_i, y_i)$. Similarly, the thickness line is defined by another six control points, $t_i(x_i y_i)$. Each set of control points can be manipulated independently, thereby decoupling the variation in camber and thickness. The control points for the camber line and thickness line include four fixed endpoints (c_0, c_5) , (t_0, t_5) at the leading and trailing edges, and eight intermediate points (c_1–c_4), (t_1–t_4) whose x- and y-coordinates serve as controllable points. All control points and generated camber line and thickness lines are shown in Figure 4.2. Figure 4.3 illustrates the resulting 5% cambered plate airfoil [9] generated using the IGP

method. This parameterization framework provides sufficient geometric flexibility for optimization while maintaining physically realizable airfoil shapes.

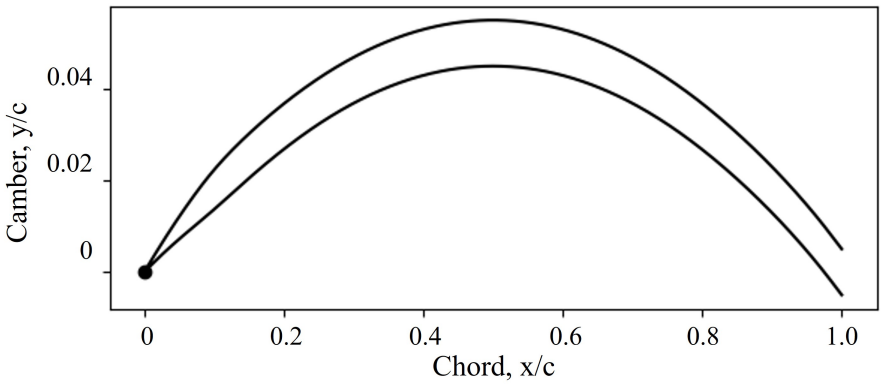

Figure 4.3: 5% cambered plate airfoil geometry generated by IGP with NURBS.

4.3 Fitness Function

The fitness function used in this optimization framework is defined to minimize $C_{d_{mean}}$ within a prescribed design lift coefficient range. This approach ensures that the optimized airfoil does not only exhibit low drag at a single operating point but also maintains robust aerodynamic performance across the entire lift coefficient range relevant to hover conditions. The evaluation process begins by performing DNS analyses at multiple angles of attack to obtain sectional lift (C_l) and drag (C_d) data. The discrete C_l, C_d data points are then interpolated using a spline method to generate a continuous drag polar. Finally, $C_{d_{mean}}$ is calculated by integrating the interpolated drag polar across the specified lift coefficient range defined by $C_{l_{lower}}$ and $C_{l_{upper}}$. By minimizing $C_{d_{mean}}$, the optimization process ensures that the resulting airfoil delivers consistently high aerodynamic efficiency across the entire design envelope rather than focusing on a single narrow operating point.

Chapter 5

Optimization Task

In this study, the planform of the blade is fixed to that of NASA's Ingenuity rotor, and the baseline airfoil is selected as clf5605, which is the main airfoil used in Ingenuity's rotor blades and shown in Fig 3.9. Both the planform and baseline airfoil are adopted directly from Ingenuity because this helicopter has already been successfully flight-tested on Mars, providing a validated and proven geometry for powered flight in the Martian atmosphere. The design optimization therefore focuses solely on refining the airfoil geometry at selected radial stations while maintaining this validated baseline configuration. The optimization task is formulated as a single-objective optimization problem with the goal of minimizing $C_{d_{mean}}$ at each optimized radial station. To ensure structural feasibility, a geometric constraint is imposed so that the minimum thickness of trailing edge of the optimized airfoil ($t/c_{\min}$) remains larger than

that of the baseline airfoil ($t/c_{\text{min,baseline}}$). Thickness constraints are derived from the OML CAD model of Ingenuity's rotor blade.

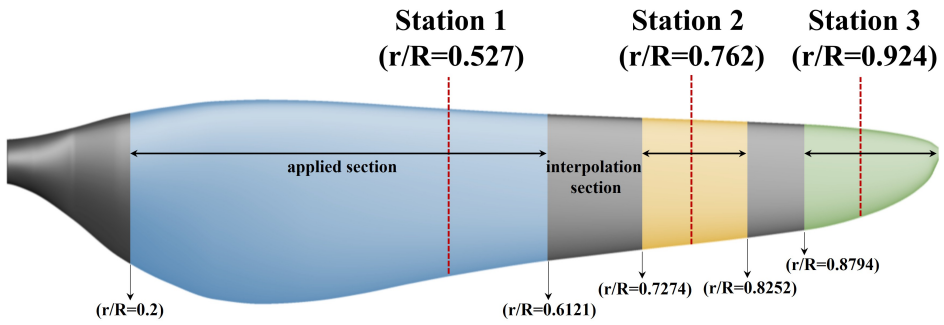

Figure 5.1: Rotor blade planform showing three radial stations for optimization.

Table 5.1: Flow conditions and design C_l range for fitness value ($C_{d_{mean}}$) of each Station.

Variable	Station 1	Station 2	Station 3
r/R	0.5271	0.7520	0.9241
Re_c	13,790	14,845	12,822
$Mach$	0.40	0.58	0.70
$C_{l_{\text{lower bound}}}$	0.60	0.55	0.45
$C_{l_{\text{upper bound}}}$	1.00	0.95	0.85
$t/c_{\text{min,baseline}}$	0.51%	0.68%	0.96%

The design target thrust for the rotor is set to 7.35 N ($C_T/\sigma = 0.125$), which corresponds to the required thrust for hover derived from the conceptual design of the MAE. To meet this target, the sectional load distribution of the baseline rotor blade is analyzed, and three representative radial stations are selected for optimization: Station 1 at $r/R = 0.527$, Station 2 at $r/R = 0.752$, and Station 3 at $r/R = 0.924$ which are shown in Figure 5.1. The intermediate sections

between these stations are determined through interpolation. The flow conditions and evaluation ranges for the fitness function ($C_{d_{mean}}$) are summarized in Table 5.1. The Reynolds numbers and Mach numbers at the three stations range from approximately 12,800 to 14,900 and 0.4 to 0.7, respectively. For each station, the lift coefficient range ($C_{l_{\text{lower}}} \leq C_l \leq C_{l_{\text{upper}}}$) is selected based on the operating conditions derived from the baseline blade's sectional load distribution in hover. These bounds ensure that the optimized airfoils achieve improved aerodynamic performance within the practical operating envelope of the rotor.

Table 5.2: Design variables and design space.

Design variable	Control point	Lower bound	Upper bound
Design variable$_1$	x_1 for c_1	0.01	0.1
Design variable$_2$	y_1 for c_1	-0.05	0.05
Design variable$_3$	x_2 for c_2	0.1	0.4
Design variable$_4$	y_2 for c_2	0	0.1
Design variable$_5$	x_3 for c_3	0.4	0.75
Design variable$_6$	x_4 for c_4	0.75	0.95
Design variable$_7$	y_4 for c_4	-0.05	0.05
Design variable$_8$	y_0 for t_0	-0.05	0.05
Design variable$_9$	x_1 for t_1	-0.05	0.05

The airfoil geometry is parameterized using a total of 10 design variables, which independently control the camber line and thickness distribution through NURBS representation. In principle, there are four adjustable control points for the camber line and four for the thickness line, excluding the fixed points at the leading edge (LE) and trailing edge (TE). This reduction in degrees of freedom decreases the total number of design variables from 12 to 10, thereby

improving the accuracy of the surrogate model during the optimization process with the same number of design sample points. This decision is based on several pre-optimization studies, which have shown that an excessive number of design variables can hinder convergence and lead to unnecessarily complex shapes. By coupling y_3 and y_2, the parameterization remains flexible enough to explore a broad design space while maintaining computational efficiency. The design variable bounds are selected to ensure feasible geometries. The x-coordinates of the camber control points vary from 0.01 to 0.95 in normalized chordwise location, while the y-coordinates are bounded between -0.05 and 0.1 relative to the chord length. Similarly, the thickness line control points follow comparable bounds in the y- or x-direction to maintain appropriate leading and trailing edge geometry (Table 5.2). All aerodynamic analyses are performed under the atmospheric conditions of Mars. Compared to standard sea-level conditions on Earth, the Martian atmosphere is characterized by significantly lower density (0.017 kg/m^3) and temperature (223 K), resulting in a reduced speed of sound (220 m/s). These properties are fully reflected in the aerodynamic performance evaluations carried out for each candidate airfoil during the optimization.

Chapter 6

Airfoil Optimization Results

The airfoil optimization at three radial stations result in significant improvements in aerodynamic efficiency, reduction of viscous drag that dominate at low Reynolds numbers. Table 6.1 and Table 6.2 summarizes geometric variations and the aerodynamic performance improvements of the optimized airfoils at the three radial stations. The optimized airfoils at Station 1 and Station 2 which are shown in Figure6.1, exhibit a Sharp Raised-Lip (SRL) shape, while the optimal airfoil at Station 3 features a thin-cambered shape. The maximum thickness of all airfoils has been fixed at 1% of the chord. This decision has been made because the initial design-space exploration has revealed a clear trend: the thinner the airfoil, the lower $C_{d_{mean}}$, which serves as the fitness value in this study. Therefore, the thickness has been fixed at 1%c, the minimum value that still ensures manufacturability. This section presents the findings from the

DNS-based optimization, including both quantitative performance metrics and qualitative flow-field analysis. Furthermore, because these airfoils have been designed to enhance the hovering performance of the rotor, a detailed performance comparison between the baseline airfoils and the optimized airfoils under lift-trimmed conditions is also conducted.

Table 6.1: Geometrical comparison of baseline clf5605 airfoils and optimized airfoils at each station.

Station	Airfoil	Max. Camber (f/c)	Max. Thickness (t/c)	Thickness (t/c) @ TE
1	clf5605 (baseline)	0.050	0.051	0.005
	Optimized airfoil	0.051	0.010	0.005
2	clf5605 (baseline)	0.050	0.051	0.007
	Optimized airfoil	0.037	0.010	0.009
3	clf5605 (baseline)	0.050	0.052	0.010
	Optimized airfoil	0.025	0.010	0.010

Table 6.2: Performance comparison of baseline clf5605 airfoils and optimized airfoils at each station.

Station	Airfoil	$C_{d_{mean}}$	Improvement [%]
1	clf5605 (baseline)	0.0455	-
	Optimized airfoil	0.0359	21.1
2	clf5605 (baseline)	0.0458	-
	Optimized airfoil	0.0344	24.8
3	clf5605 (baseline)	0.0517	-
	Optimized airfoil	0.0368	28.7

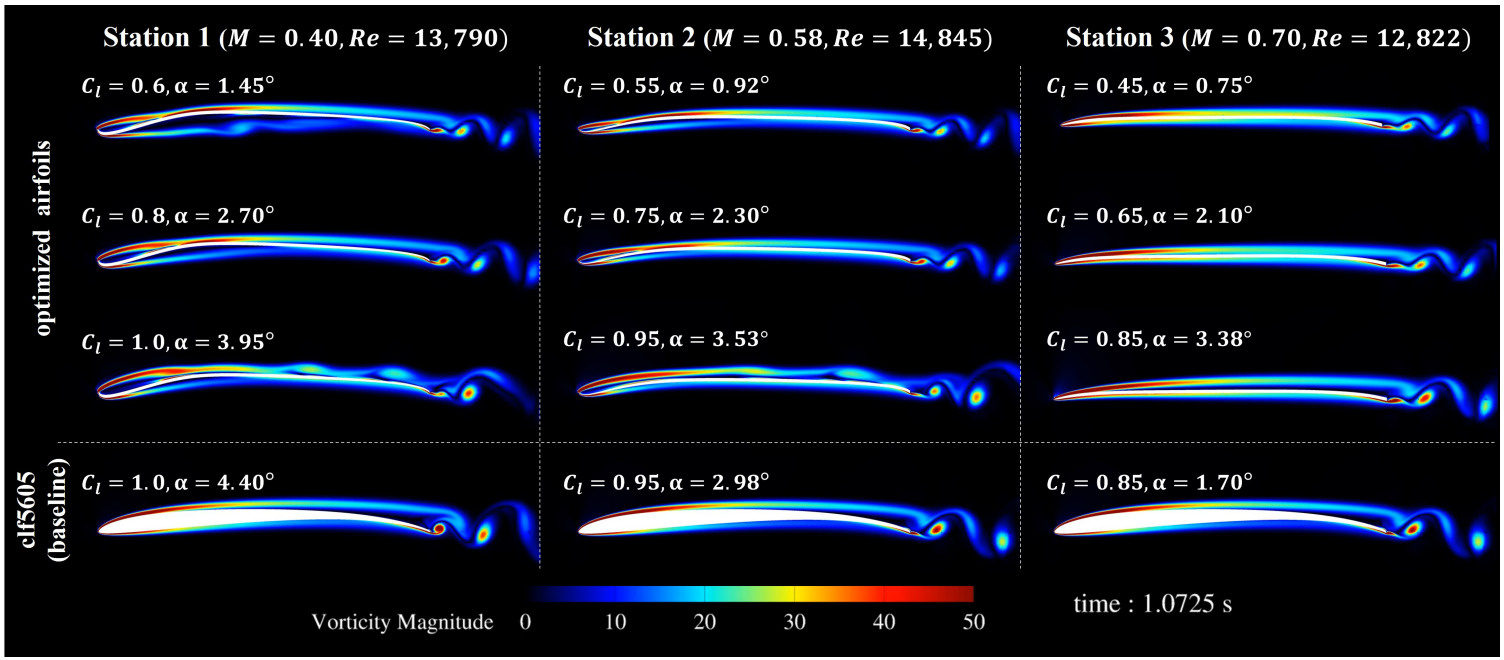

Figure 6.1: Instantaneous flow field (non-dimensional vorticity magnitude) comparing baseline clf5605 airfoils and optimized airfoils for each station.

6.1 Optimization Results for Station 1 ($r/R = 0.527$)

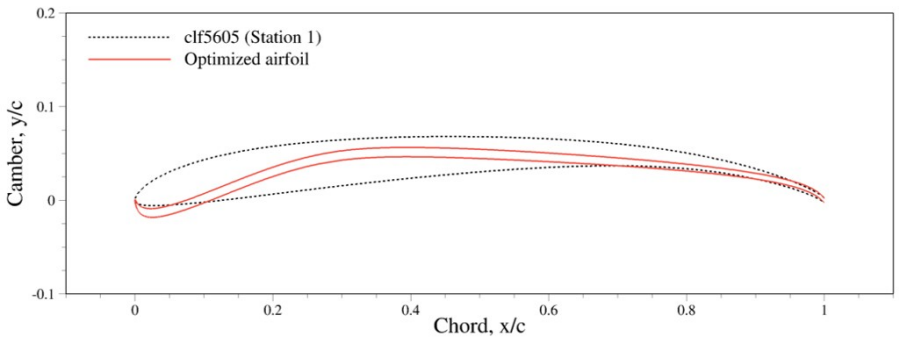

Figure 6.2: Optimized airfoil geometry at station 1 ($r/R = 0.527$).

The optimized airfoil at Station 1 exhibits a SRL feature near the leading edge, as shown in Figure 6.2. Compared to the baseline clf5605 airfoil, the camber line is slightly reversed in the forward chord region ($x/c < 0.2$), while the maximum camber and trailing-edge thickness remain nearly unchanged (Table 6.1).

Figure 6.3 present the drag polar of the baseline clf5605 airfoil and optimized airfoil under the local flow condition (M=0.40, Re=13,790). The drag polar shows that the optimized airfoil achieves a drag reduction across the entire design lift coefficient range ($0.6 < C_l < 1.0$). As a result, the optimized airfoil has achieved a 21.1% reduction in mean drag coefficient ($C_{d,\text{mean}}$) compared to the baseline clf5605 airfoil.

To further clarify the drag reduction mechanism, a drag breakdown has been performed under three C_l-trimmed conditions. The time-averaged pres-

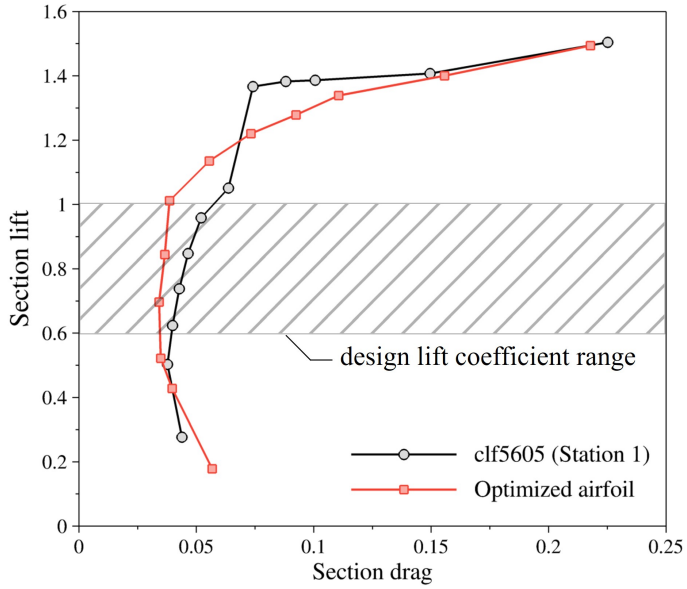

Figure 6.3: Comparison of drag polars for the baseline clf5605 airfoil and the station 1 ($r/R = 0.527$) optimized airfoil at $M = 0.40$ and $Re = 13,790$.

sure and skin friction distributions for each C_l-trimmed condition are shown in Figure 6.4, where the time averaging has been carried out over the final 25 CTU. At $C_l = 0.6$, the pressure drag increases, but the skin friction drag decreases significantly, resulting in a total drag reduction of 14%. As seen in Figure 6.4a, the adverse pressure gradient on the suction side is caused by the leading-edge separated flow impinging on the airfoil surface, as illustrated in Figure 6.5. Due to the reverse camber effect, the optimized airfoil generates surface pressure vectors near the leading edge that are tilted in the drag direction. Consequently, the pressure drag of the optimized airfoil increases by 51% relative to the baseline clf5605 airfoil. Figure 6.5 further reveals that the shear layers separate at the leading edge on both the suction and pressure sides.

On the suction side, this separation leads to the formation of a Laminar Separation Bubble (LSB). As shown in Figure 6.4a, the suction side experiences very low skin friction values near the leading edge because of the LSB, while the pressure side also shows very low skin friction values $x/c < 0.6$ due to the separated shear layer. Overall, the friction drag decreases by 68% compared to the baseline clf5605 airfoil.

A similar trend is observed at higher lift coefficients ($C_l = 0.8$ and 1.0), as shown in Figure 6.4b and 6.4c. At $C_l = 1.0$, the separated shear layer of the optimized airfoil develops into large-scale shed vortices without transition to small-scale turbulence, as illustrated in Figure 6.6. This phenomenon occurs because the strong velocity difference across the shear layer triggers Kelvin–Helmholtz instabilities. In addition, at higher angles of attack, the separated flow from the leading edge no longer impinges on the airfoil surface but instead forms a larger LSB, allowing the optimized airfoil to maintain lower suction-side pressures than the baseline clf5605 airfoil. As a result, both the skin friction drag and the pressure drag decrease, leading to the largest total drag reduction of 31% within the design range.

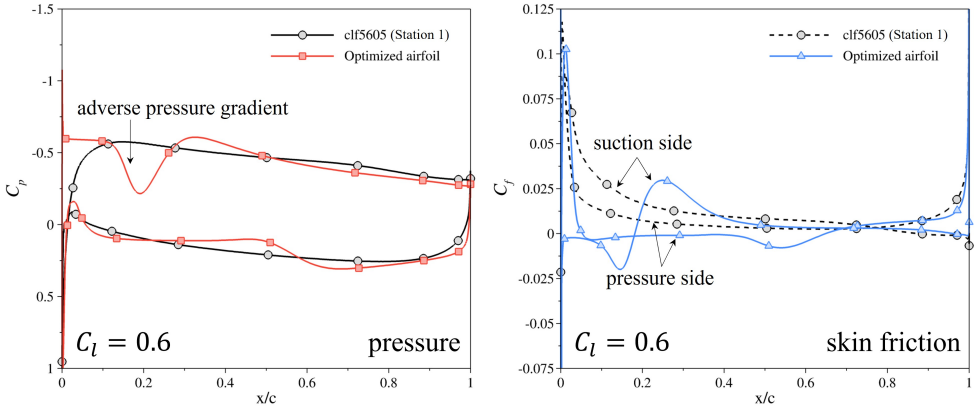

(a) Pressure (left) and skin friction (right) coefficients at $C_l = 0.6$

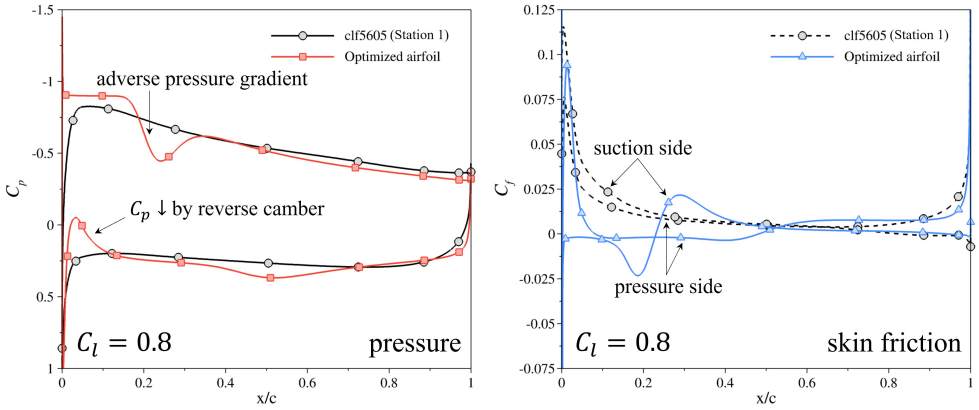

(b) Pressure (left) and skin friction (right) coefficients at $C_l = 0.8$

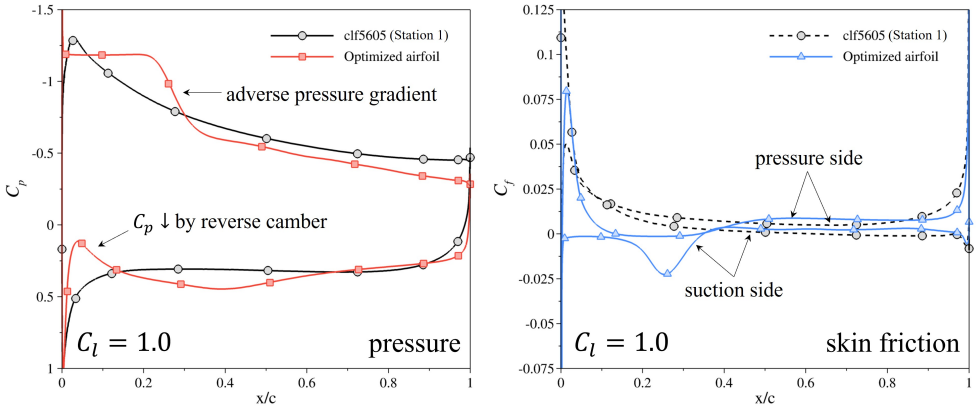

(c) Pressure (left) and skin friction (right) coefficients at $C_l = 1.0$

Figure 6.4. Comparison of pressure coefficient (C_p) and skin friction coefficient (C_f) distributions for the baseline clf5605 airfoil and station 1 ($r/R = 0.527$) optimized airfoil at $M = 0.40$ and $Re = 13,790$.

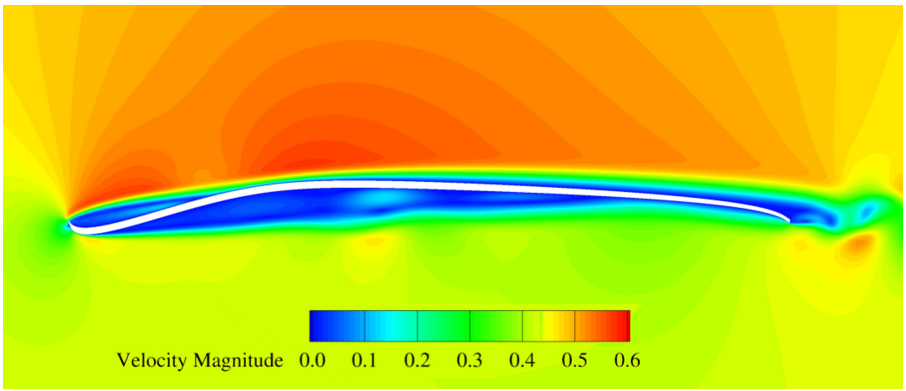

Figure 6.5: Instantaneous flow field (non-dimensional velocity) for station 1 ($r/R = 0.527$) optimized airfoil at $C_l = 0.6$.

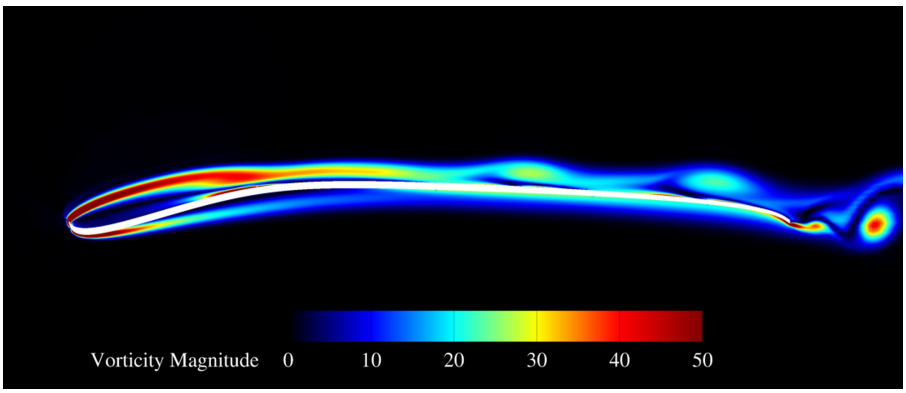

Figure 6.6: Instantaneous flow field (non-dimensional vorticity magnitude) for station 1 ($r/R = 0.527$) optimized airfoil at $C_l = 1.0$.

6.2 Optimization Results for Station 2 ($r/R = 0.752$)

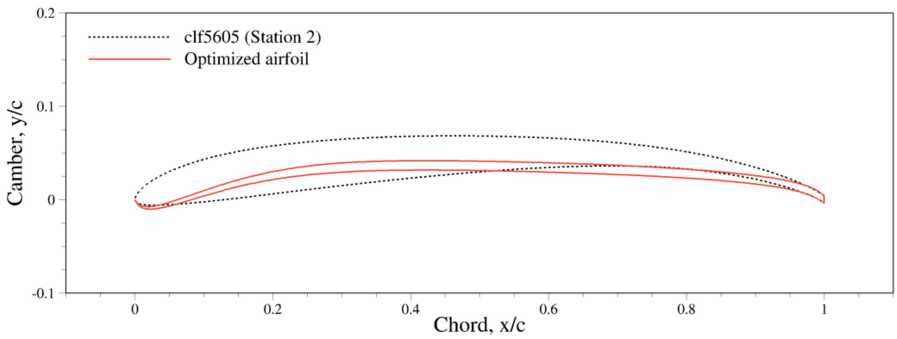

Figure 6.7: Optimized airfoil geometry at station 2 ($r/R = 0.752$).

Similar to Station 1, the optimized airfoil at Station 2 (Figure 6.7) achieves a significant improvement in aerodynamic performance, reducing $C_{d,\text{mean}}$ by 24.8% compared to the baseline clf5605 airfoil within the design lift coefficient range ($0.55 < C_l < 0.95$). The optimized geometry exhibits a noticeably reduced camber across the chord compared to both the baseline clf5605 airfoil and the Station 1 optimized airfoil (Figure 6.2), while the maximum thickness remains unchanged (Table 6.1).

The drag polar shown in Figure 6.8 indicate that the optimized airfoil achieves lower drag across the entire design lift coefficient range. At $C_l = 0.55$ and $C_l = 0.75$, the time-averaged pressure distributions of the optimized airfoil demonstrate a similar trend, and the pressure distribution at $C_l = 0.75$ is shown in Figure 6.9. The reduced camber of the optimized airfoil increases the pressure on the suction side for $x/c > 0.3$ and on the pressure side for

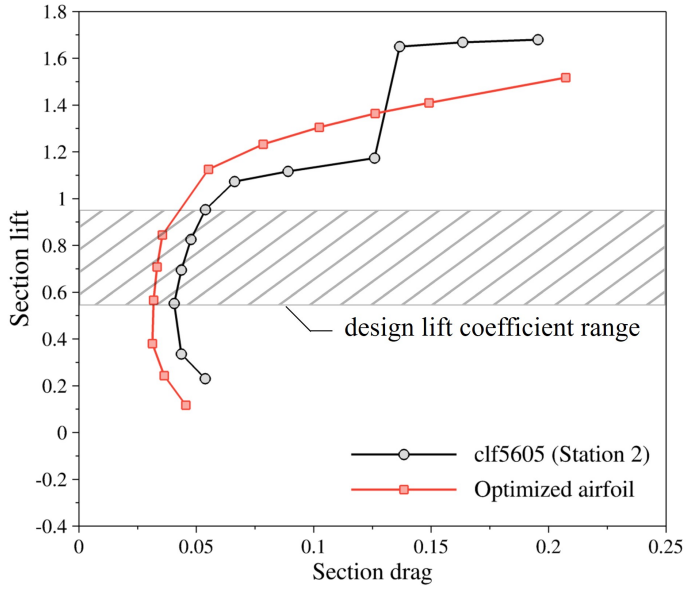

Figure 6.8: Comparison of drag polars for the baseline clf5605 airfoil and the station 2 ($r/R = 0.752$) optimized airfoil at $M = 0.58$ and $Re = 14,845$.

$x/c < 0.5$, and the corresponding pressure vectors are presented in Figure 6.9. Because the pressure vectors on the pressure side tilt toward the leading edge, the pressure drag is reduced. For the skin friction drag, a similar behavior to that of the Station 1 optimized airfoil has been observed. The flow separated at the leading edge by the SRL feature causes the skin friction to decrease significantly compared to the baseline clf5605 airfoil, resulting in a 35–75% reduction in skin friction drag.

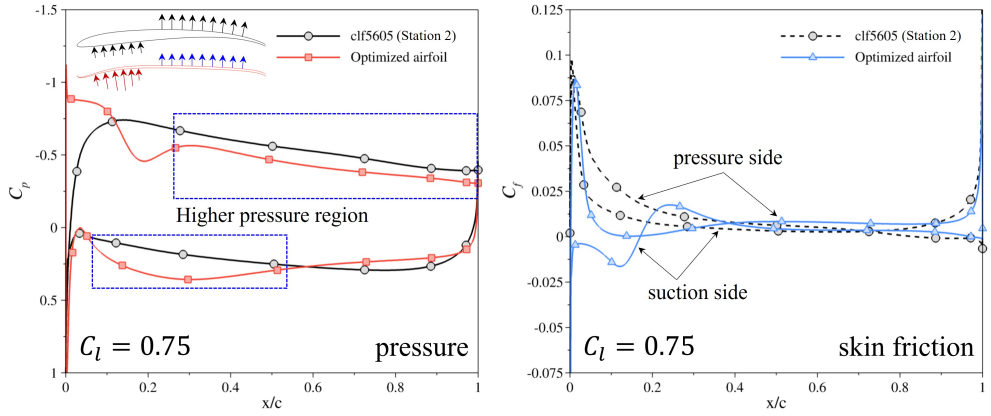

Figure 6.9: Comparison of C_p and C_f distributions for the baseline clf5605 airfoil and station 2 ($r/R = 0.752$) optimized airfoil at $C_l = 0.75$, $M = 0.58$ and $Re = 14,845$.

6.3 Optimization Results for Station 3 ($r/R = 0.924$)

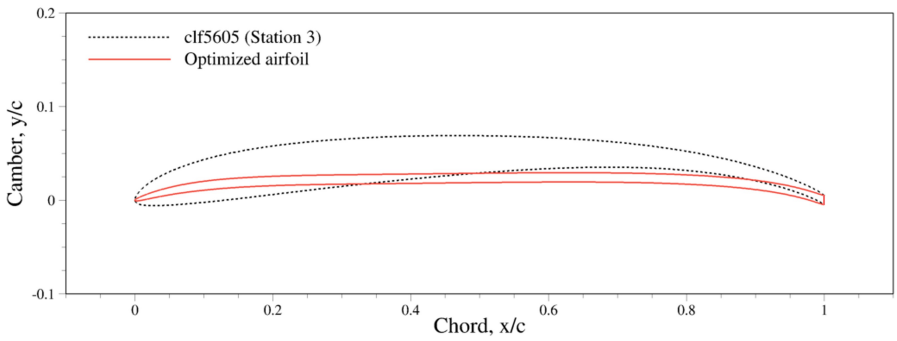

Figure 6.10: Optimized airfoil geometry at station 3 ($r/R = 0.924$)

The optimized airfoil at Station 3 exhibits a thin-cambered shape, as shown in Figure 6.10. Compared to the baseline clf5605 airfoil, the camber line and thickness have been significantly reduced, particularly in the forward and mid-chord regions, resulting in a more slender geometry. While the trailing-edge thickness remains unchanged, the maximum camber and thickness values are notably smaller (Table 6.1). This geometric modification contributes to a substantial drag reduction across the entire design lift coefficient range ($0.45 < C_l < 0.85$), as evidenced by the drag polar in Figure 6.11. The optimized airfoil achieves a 28.7% reduction in $C_{d_{mean}}$ compared to the baseline airfoil, the largest improvement observed among the three stations.

At $C_l = 0.55$, the optimized airfoil achieves the greatest total drag reduction of 30.4%, primarily driven by a 69.8% reduction in pressure drag. This improvement is attributed to the significant shift of the high-pressure region

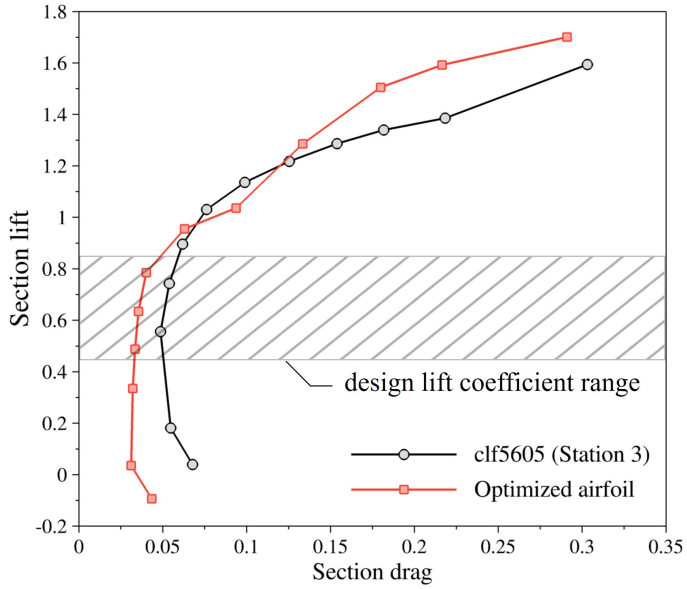

Figure 6.11: Comparison of drag polars for the baseline clf5605 airfoil and the station 3 ($r/R = 0.924$) optimized airfoil at $M = 0.70$ and $Re = 12,822$.

in front of the leading edge towards the pressure side(lower surface of airfoil), as seen in Figure 6.12, which reduces the adverse pressure gradient on the suction side. However friction drag increases by 40% due to the sharper and thin cambered leading edge and more attached boundary layer, the overall drag reduction remains dominant.

At $C_l = 0.75$ and $C_l = 0.95$, a similar mechanism is observed, with a 29.3% and 23.2% reduction in total drag for each condition. thin-cambered optimized airfoil's geometry effectively mitigates high-pressure region and suppresses unsteady flow phenomena, resulting in significant drag reductions at all trimmed lift coefficients. This demonstrates the crucial role of camber and thickness reduction at the outer blade sections, where the local Mach number and Reynolds

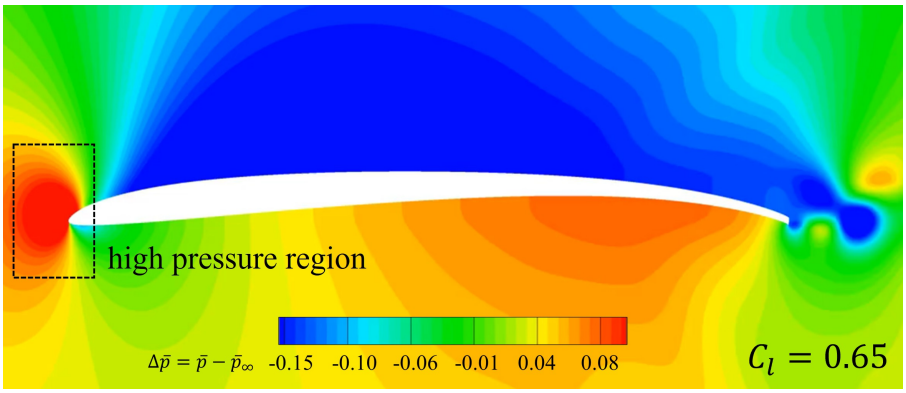

(a) Instantaneous flow field for baseline clf5605 airfoil

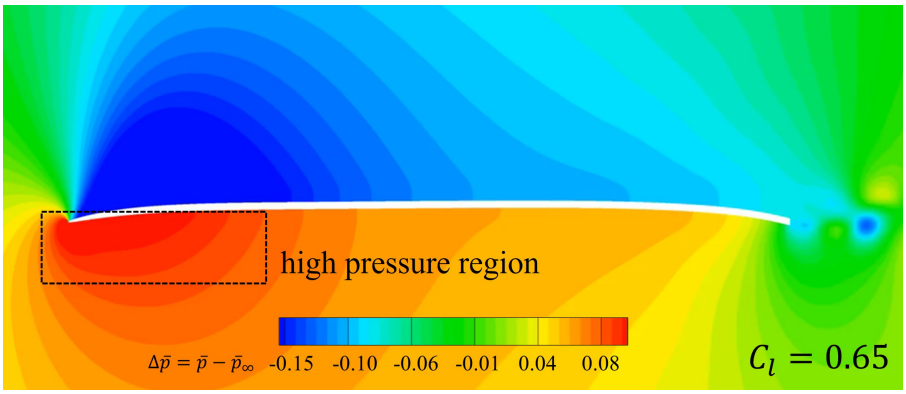

(b) Instantaneous flow field for station 3 optimized airfoil

Figure 6.12. Instantaneous flow field (non-dimensional gage pressure) for station 3 ($r/R = 0.924$) optimized airfoil at $C_l = 0.65$.

number are highest.

Chapter 7

3D Rotor Aerodynamics with Optimized Airfoils

The final phase of this study has applied the optimized airfoils derived from the 2D DNS-based station-wise optimization to a full-scale 3D single-rotor model of the Ingenuity Mars Helicopter. The rotor planform geometry reflecting the optimized airfoil shapes is shown in Figure 7.1, where the SRL airfoils can be seen applied across the inboard and midboard regions. This section presents the results of the 3D DNS simulations, including overall performance metrics, analysis at the thrust-trimmed condition, and a detailed characterization of the flow structures around the optimized rotor.

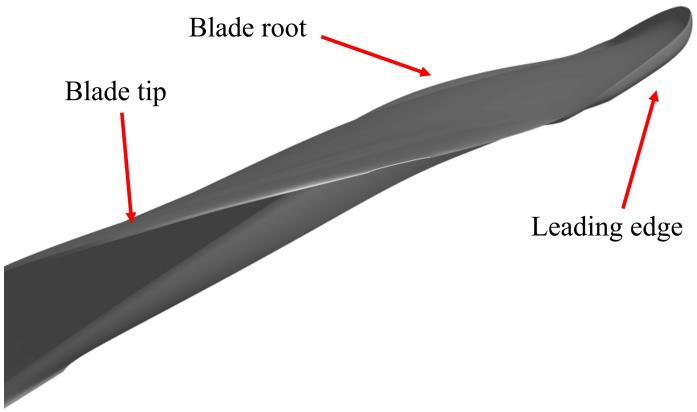

Figure 7.1: Rotor blade geometry incorporating the optimized airfoils.

7.1 Rotor Performance at Design Thrust Condition ($C_T/\sigma = 0.125$)

The aerodynamic performance of the baseline Ingenuity single rotor is compared with that of the optimized rotor in which the optimized airfoils from the 2D design process are applied. Both rotors are trimmed to match the design thrust condition ($C_T/\sigma = 0.125$) under the design tip Mach number and Reynolds number ($M_{tip} = 0.76, Re = 21,772$). The comparison reveals that both rotors exhibit nearly identical sectional thrust distributions along the span, as shown in Figure 7.2a. This indicates that the optimized airfoils do not negatively impact the lift-carrying capability of the rotor blades at the same station. However, notable differences arise in the sectional torque and pitching moment distributions. In the outboard region ($r/R > 0.6$), the optimized rotor demonstrates a clear reduction in sectional torque compared to the baseline Ingenuity single rotor, as illustrated in Figure 7.2b. This reduction is attributed to the lower profile drag characteristics of the optimized airfoils, which contribute to a decrease in the required power. Similarly, the sectional pitching moment is consistently lower in the optimized rotor at $r/R > 0.6$ (7.2c). This behavior stems from the refined camber and thickness distributions of the optimized airfoils, which mitigate nose-down pitching tendencies in the outboard blade sections. As a result of these aerodynamic improvements, the optimized rotor achieves a higher figure of merit (FM) compared to the baseline rotor. The FM of the optimized rotor is 0.588, which corresponds to a 6.9% increase

over the baseline Ingenuity single rotor (FM = 0.549) while maintaining the same design thrust. This performance gain demonstrates the positive impact of the optimized airfoils on the overall efficiency of the rotor system.

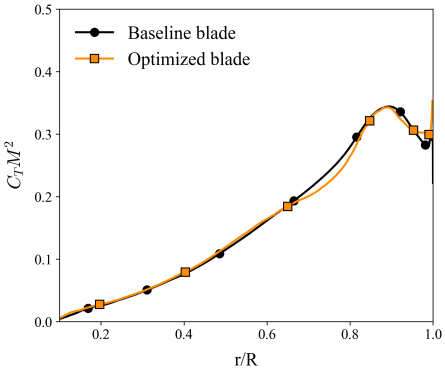

(a) Sectional thrust distributions

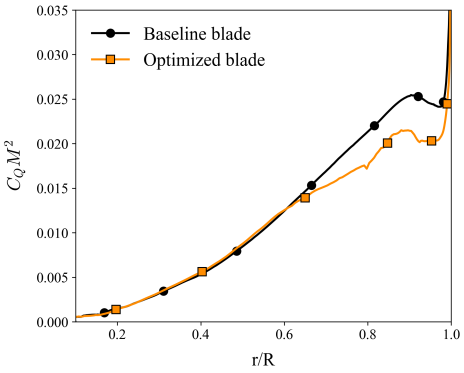

(b) Sectional torque distributions

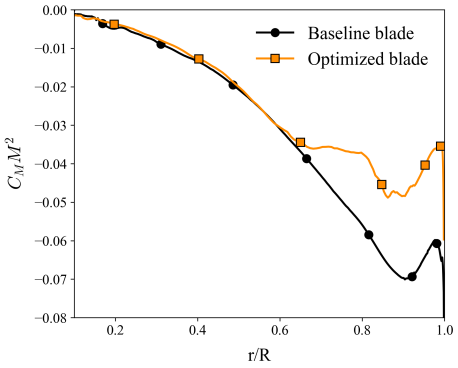

(c) Sectional pitching moment distributions

Figure 7.2. Sectional performance comparison results for baseline Ingenuity singe rotor and optimized rotor in hover at $C_T/\sigma = 0.125$.

7.2 Comparison of 2D and 3D Behaviors of Optimized Airfoils

This section investigates the aerodynamic behavior of the optimized airfoils in a 3D rotor environment and compares it with the behavior predicted by 2D simulations. The purpose is to determine whether the performance and flow characteristics observed during the 2D optimization stage are maintained under actual rotor operating conditions. The pressure coefficient (C_p) and skin friction coefficient (C_f) distributions extracted from the 3D rotor simulation at Station 1 are compared with the corresponding distributions obtained from the 2D simulation at $C_l = 0.8$. The distributions obtained from 3D rotor simulations and 2D simulations are in close agreement. This indicates that the optimized airfoil behavior in the 2D environment is well preserved in the 3D rotor blade at station 1. station 2 also shows results similar to Station 1, with 2D and 3D behaviors closely matching.

Unlike Stations 1 and 2, the aerodynamic behavior at Station 3 differs noticeably between the 2D and 3D analyses. Figures 7.3 compares the distributions of C_p obtained from the 2D simulation and the 3D rotor simulation. The differences are further clarified by the vorticity contours of the optimized rotor at Station 3, shown in Figure 7.4. In the 3D rotor simulation, the optimized rotor exhibits large-scale vortex shedding at the blade tip, which is absent in the 2D simulation.

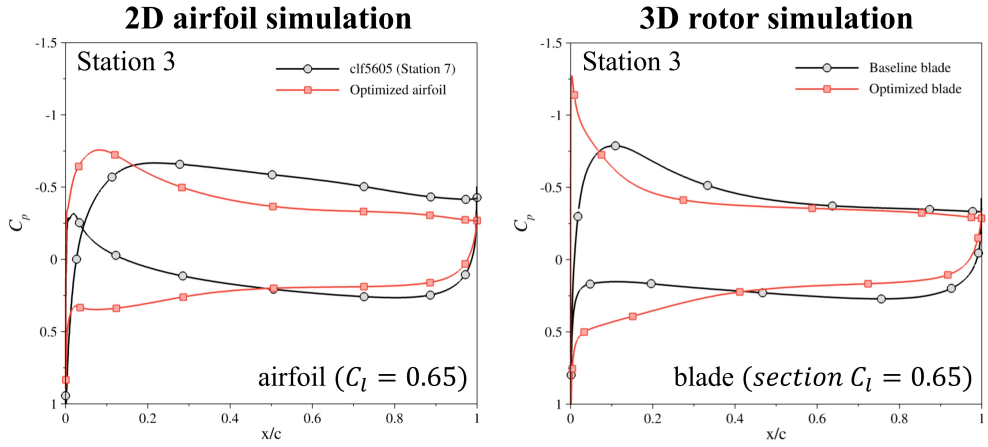

Figure 7.3: Comparison of C_p distributions between 2D airfoil simulation ($C_l = 0.65$) and 3D rotor simulation at station 3 ($r/R = 0.924$) with the baseline and optimized configurations.

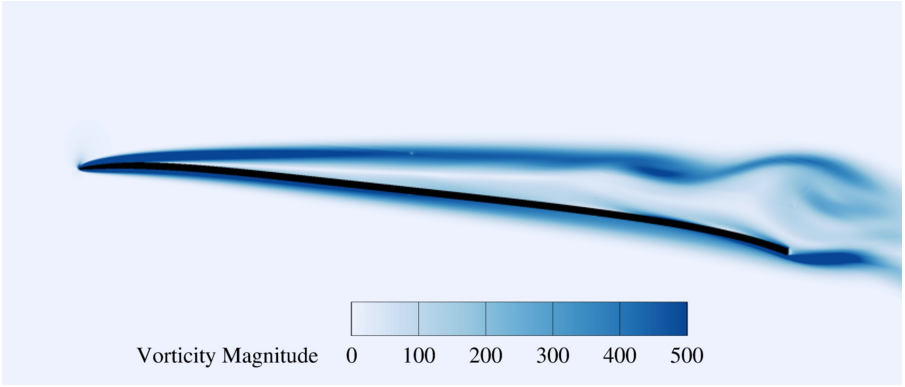

Figure 7.4: Sliced instantaneous flow field (non-dimensional vorticity magnitude) at station 3 ($r/R = 0.924$) and $\psi = 0°$.

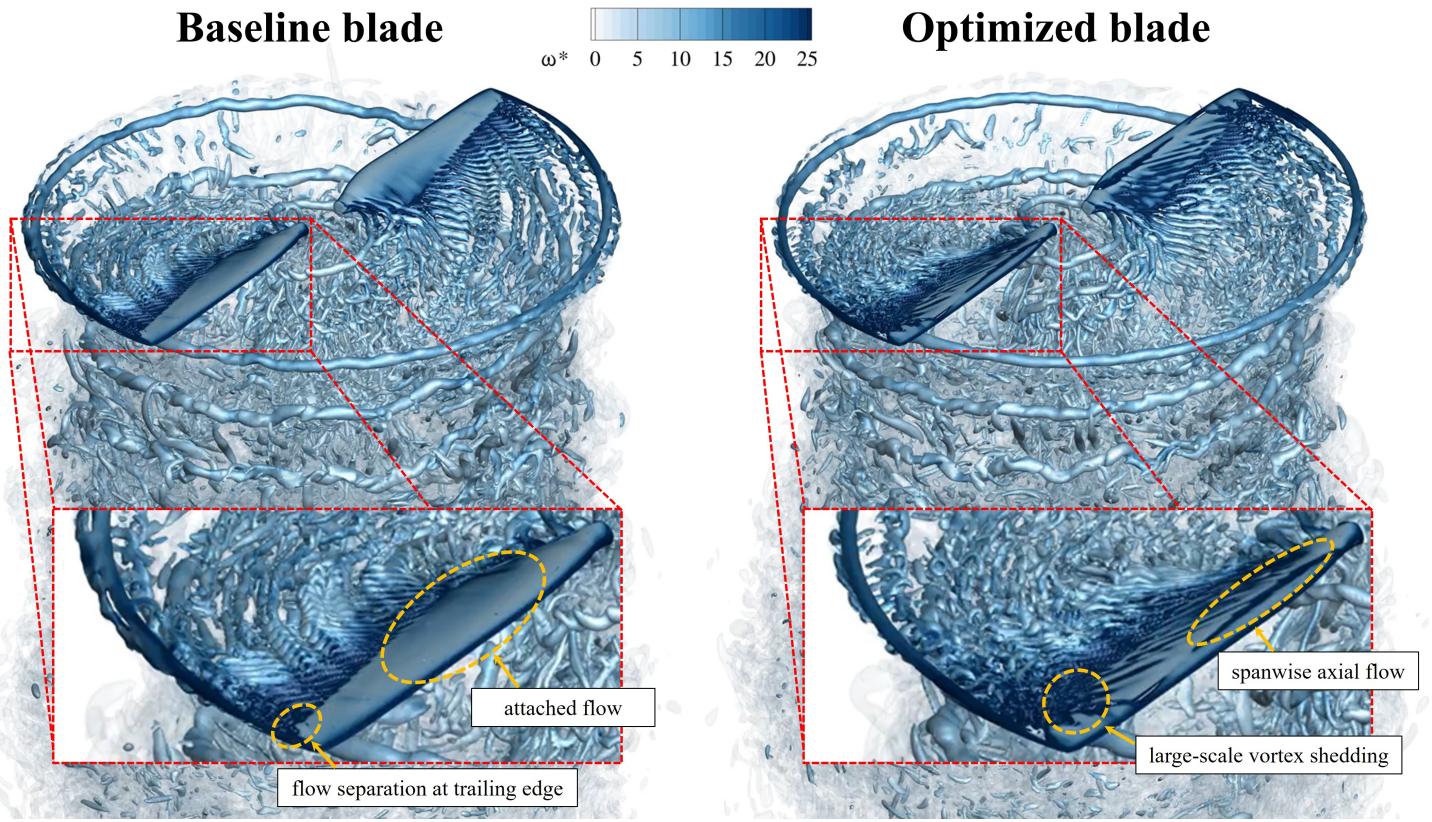

Figure 7.5: Instantaneous Q-criterion colored by non-dimensional vorticity magnitude for the baseline Ingenuity single rotor and optimized rotor at $\psi = 0°$.

To obtain a clearer understanding of the observed differences, Figure 7.5 shows the Q-criterion iso-surfaces for both the baseline Ingenuity single rotor and the optimized rotor. Due to the low Reynolds number environment, tip vortices generated by the rotor dissipate within three revolutions. The overall wake structure is similar between the baseline and optimized rotors; however, detailed inspection of the flow near the blade surface reveals distinct differences. For the baseline Ingenuity single rotor, no significant flow separation is observed along the blade surface except near the tip trailing edge. In contrast, the optimized rotor shows that the SRL airfoils at the inboard and midboard sections trigger leading-edge flow separation, generating spanwise flow. This spanwise flow interacts with the separated flow near the blade tip, leading to instabilities and the development of large-scale vortex shedding. This phenomenon explains why the Station 3 airfoil displays different aerodynamic behavior in the 3D rotor simulation compared to the 2D simulation.

7.3 Off-Design Analysis Results

Lastly, to evaluate rotor performance at thrust conditions other than the design thrust, an off-design analysis is conducted for both the baseline Ingenuity single rotor and the optimized rotor, and the results are summarized in Figure 7.6. It compares blade loading (C_T/σ), power coefficient (C_P/σ), and FM. At the same collective pitch angle, the optimized rotor produces slightly less thrust than the baseline rotor due to the reverse camber effect of the SRL airfoils. However, at the design thrust condition ($C_T/\sigma = 0.125$), the power coefficient is reduced by approximately 7.6%, leading to an overall 7% improvement in FM. It is also noteworthy that the margin between the design thrust condition and the maximum FM is smaller for the optimized rotor, indicating an earlier onset of stall compared to the baseline Ingenuity single rotor.

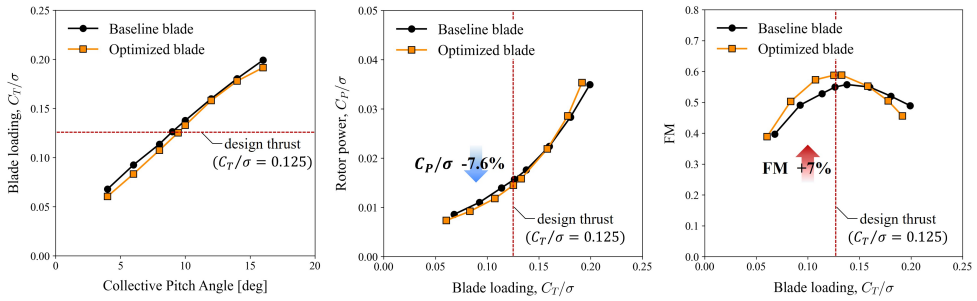

Figure 7.6: Off-design analysis results for the baseline Ingenuity single rotor and opimized rotor in hover.

Instantaneous sectional pressure and skin friction contours at $\theta_0 = 12°$ in the post-stall range are shown in Figure 7.7. In this regime, the optimized ro-

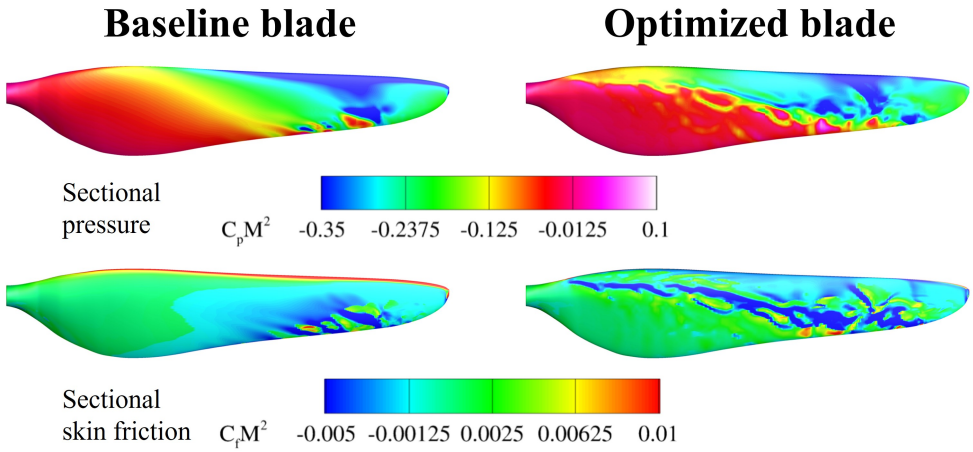

Figure 7.7: Comparison of sectional pressure and skin friction contours between the baseline and optimized blades at $\theta_0 = 12°$.

tor begins to underperform relative to the baseline Ingenuity single rotor. The onset of stall occurs earlier, and highly complex unsteady flow structures develop across the blade surface. These unsteady flow features result in increased sectional skin friction at higher pitch angle. In particular, the optimized rotor experiences flow instabilities that reduce its aerodynamic efficiency at $\theta_0 \geq 12°$.

Chapter 8

Conclusion

The optimized airfoils for a Mars helicopter rotor operating under low Reynolds number conditions have been successfully derived. The accuracy of CFD simulations in this challenging flow regime has been ensured by performing and validating both 2D airfoil and 3D rotor Direct Numerical Simulations (DNS) against experimental data and other CFD solvers. The design space has been broadened by defining airfoil geometries using an IGP with NURBS parameterization method. The optimization has been conducted to minimize the mean drag of airfoils at the hover thrust condition of the MAE octocopter derived from the conceptual design, and three optimized airfoils for different radial stations have been obtained. The physical mechanisms behind the reduced drag observed in the optimized airfoils within the design lift coefficient range have been identified through lift-trim analyses. Finally, these airfoils have

been incorporated into the baseline Ingenuity single rotor to perform 3D rotor aerodynamic analyses. The main conclusions are summarized as follows:

1. High-performance airfoils were derived for three radial stations. The optimized airfoils achieved a 21–28% reduction in drag compared to the baseline clf5605 airfoil at the same lift coefficient. These improvements were obtained using a station-wise 2D DNS-driven optimization process, demonstrating the effectiveness of the Sharp Raised-Lip (SRL) and thin-cambered airfoil configurations for Martian flight conditions.

2. The mechanism behind the aerodynamic improvements was identified. The SRL geometry induces controlled shear-layer separation at the leading edge, forming a leading-edge laminar separation bubble (LSB) that reduces skin friction drag. Under low Reynolds number conditions, skin friction accounts for 10–50% of total drag, and the LSB's contribution to delaying separation and reducing viscous losses plays a key role in the performance gains.

3. Rotor-level 3D aerodynamic analysis revealed consistency with 2D optimization for most stations except for the tip region. The optimized airfoils for Stations 1 and 2 showed close agreement between 2D and 3D aerodynamic behaviors, confirming the robustness of the optimization process. However, Station 3, located near the blade tip, exhibited distinct aerodynamic characteristics in the 3D rotor environment, including the onset

of large-scale vortex shedding not captured in 2D simulations.

4. The optimized rotor demonstrated improved performance near the design thrust condition. At the thrust-trimmed condition ($C_T/\sigma = 0.125$), the optimized rotor exhibited a 7% increase in Figure of Merit (FM) and a 7.6% reduction in power coefficient relative to the baseline Ingenuity rotor. In the pre-stall range ($\theta_0 = 4^\circ \sim 10^\circ$), the optimized rotor consistently outperformed the baseline rotor with stable aerodynamic behavior and reduced unsteadiness. However, the optimized rotor showed a reduced stall margin, with earlier onset of unsteady flow at higher collective pitch angles ($\theta_0 > 10^\circ$).

Nevertheless, the framework also has some limitations. Additional iterative optimization is required to fully account for 3D effects in the tip region, particularly to mitigate large-scale vortex shedding observed at Station 3. Furthermore, future studies should verify the manufacturability and structural feasibility of the optimized designs and evaluate their performance under forward flight conditions to ensure robustness across all mission profiles.

Chapter 9

References

[1] P. M. Munday, K. Taira, T. Suwa, D. Numata, and K. Asai, "Nonlinear lift on a triangular airfoil in low-reynolds-number compressible flow," vol. 52, no. 3, pp. 924–931. [Online]. Available: https://arc.aiaa.org/doi/10.2514/1.C032983

[2] W. J. F. Koning, E. A. Romander, and W. Johnson, "Optimization of low reynolds number airfoils for martian rotor applications using an evolutionary algorithm," in *AIAA Scitech 2020 Forum*. American Institute of Aeronautics and Astronautics. [Online]. Available: https://arc.aiaa.org/doi/10.2514/6.2020-0084

[3] L. Caros, O. Buxton, T. Shigeta, T. Nagata, T. Nonomura, K. Asai, and P. Vincent, "Direct numerical simulation of flow over a triangular airfoil

under martian conditions," *AIAA Journal*, vol. 60, no. 7, pp. 3961–3972, 2022.

[4] W. J. F. Koning and M. Dominguez, "Mars helicopter ingenuity rotor geometry," *NASA/TM-20240001510*, 2024.

[5] W. J. F. Koning, B. G. Allan, E. A. Romander, and W. Johnson, "Comparing 3d and 2d CFD for mars helicopter ingenuity rotor performance prediction," in *49th European Rotorcraft Forum 2023*. Deutsche Gesellschaft für Luft- und Raumfahrt - Lilienthal-Oberth e.V., Bonn.

[6] B. Balaram, T. Canham, C. Duncan, H. F. Grip, W. Johnson, J. Maki, A. Quon, R. Stern, and D. Zhu, "Mars helicopter technology demonstrator," in *2018 AIAA Atmospheric Flight Mechanics Conference*. American Institute of Aeronautics and Astronautics. [Online]. Available: https://arc.aiaa.org/doi/10.2514/6.2018-0023

[7] T. Tzanetos, M. Aung, J. Balaram, H. F. Grip, J. T. Karras, T. K. Canham, G. Kubiak, J. Anderson, G. Merewether, M. Starch, M. Pauken, S. Cappucci, M. Chase, M. Golombek, O. Toupet, M. C. Smart, S. Dawson, E. B. Ramirez, J. Lam, R. Stern, N. Chahat, J. Ravich, R. Hogg, B. Pipenberg, M. Keennon, and K. H. Williford, "Ingenuity Mars Helicopter: From Technology Demonstration to Extraterrestrial Scout," in *2022 IEEE Aerospace Conference (AERO)*.

Big Sky, MT, USA: IEEE, Mar. 2022, pp. 01–19. [Online]. Available: https://ieeexplore.ieee.org/document/9843428/

[8] G. E. Cushing, C. H. Okubo, and T. N. Titus, "Atypical pit craters on mars: New insights from THEMIS, CTX, and HiRISE observations," vol. 120, no. 6, pp. 1023–1043. [Online]. Available: https://onlinelibrary.wiley.com/doi/abs/10.1002/2014JE004735

[9] W. J. F. Koning, E. A. Romander, and W. Johnson, "Low reynolds number airfoil evaluation for the mars helicopter rotor," in *AHS International 74th Annual Forum Technology Display*, Phoenix, Arizona, May 2018.

[10] G. Sasaki, T. Tatsukawa, T. Nonomura, A. Oyama, T. Matsumoto, and K. Yonemoto, "Multi-objective optimization of airfoil for mars exploration aircraft using genetic algorithm," vol. 12, pp. 59–64.

[11] W. J. F. Koning, E. A. Romander, and W. Johnson, "Performance optimization of plate airfoils for martian rotor applications using a genetic algorithm," in *45th European Rotorcraft Forum.*

[12] S. Kwon, Y. Hong, and K. Yee, "Aerodynamic performance of an arrow airfoil in mars environment and its optimization," in *47th European Rotorcraft Forum.*

[13] L. Caros, O. Buxton, and P. Vincent, "Optimization of triangular airfoils for martian helicopters using direct numerical simulations," vol. 61,

no. 11, pp. 4935–4945. [Online]. Available: https://arc.aiaa.org/doi/10.2514/1.J063164

[14] W. J. F. Koning, B. N. Perez Perez, H. V. Cummings, E. A. Romander, and W. Johnson, "ELISA: A tool for optimization of rotor hover performance at low reynolds number in the mars atmosphere." [Online]. Available: https://www.ingentaconnect.com/content/10.4050/JAHS.69.042005

[15] W. J. F. Koning, B. N. P. Perez, H. V. Cummings, E. A. Romander, and W. Johnson, "Overview of rotor hover performance capabilities at low reynolds number for mars exploration," in *50th European Rotorcraft Forum*.

[16] W. J. F. Koning, E. A. Romander, H. V. Cummings, B. N. Perez Perez, and P. G. Buning, "On improved understanding of airfoil performance evaluation methods at low reynolds numbers," vol. 60, no. 3, pp. 774–788. [Online]. Available: https://arc.aiaa.org/doi/10.2514/1.C037023

[17] D. Lee, S. Kwon, S. Park, and K. Yee, "Conceptual design of vtol aircraft for mars exploration," in *2023 KSAS Fall Conference*.

[18] J. Kim, S. Park, H. Kim, and K. Yee, "Object-oriented framework for aircraft conceptual and preliminary design - part i. architecture and applications," in *Asia Pacific International Symposium On Aerospace Technology (APISAT 2024)*. Adelaide, South Australia: Engineers Australia, 2024.

[19] J. Raddatz and J. K. Fassbender, *Block Structured Navier-Stokes Solver FLOWer*, N. Kroll and J. K. Fassbender, Eds. DLR, Braunschweig, German,: Springer Berlin Heidelberg, 2005.

[20] K. Kitamura and E. Shima, "Towards shock-stable and accurate hypersonic heating computations: A new pressure flux for ausm-family schemes," *Journal of Computational Physics*, vol. 245, pp. 62–83, 2013.

[21] S. Yamamoto and H. Daiguji, "Higher-order-accurate upwind schemes for solving the compressible euler and navier-stokes equations," *Computers Fluids*, vol. 22, no. 2-3, pp. 259–270, 1993.

[22] G. Wilke, "Comparisons of different spatial schemes and limiters for helicopter flows," in *New Results in Numerical and Experimental Fluid Mechanics XIII*, A. Dillmann, G. Heller, E. Krämer, and C. Wagner, Ed. Springer International Publishing, 2021, pp. 418–427.

[23] V. Vatsa, M. Carpenter, and D. Lockard, "Re-evaluation of an optimized second order backward difference (bdf2opt) scheme for unsteady flow applications," in *48th AIAA Aerospace Sciences Meeting Including the New Horizons Forum and Aerospace Exposition*, 2010.

[24] R. C. Swanson and E. Turkel, "Multistage Schemes with Multigrid for Euler and Navier-Strokes Equations: Components and Analysis," NASA Langley Research Center Hampton, VA United States,, Tech. Rep. NASA-TP-3631, 1997.

[25] G. Wilke, "Aerodynamic optimization of helicopter rotor blades using variable fidelity methods," Ph.D. dissertation, Technical Univ. of Braunschweig, 2017. [Online]. Available: https://elib.dlr.de/119358/1/FB-Wilke-2017-64.pdf[retrieved04Oct.2024]

[26] N. M. Chaderjian, "Quantitative approach for the accurate cfd simulation of hover in turbulent flow," in *International Conference on Computational Fluid Dynamics*, Maui, HI, July 2022.

[27] G. Wilke, "Variable-fidelity methodology for the aerodynamic optimization of helicopter rotors," *AIAA Journal*, vol. 57, pp. 3145–3158, 08 2019.

[28] D. Jones, M. Schonlau, and W. Welch, "Efficient global optimization of expensive black-box functions," *Journal of Global Optimization*, vol. 13, pp. 455–492, 12 1998.

[29] L. Ju, Q. Du, and M. Gunzburger, "Probabilistic methods for centroidal voronoi tessellations and their parallel implementations," *Parallel Computing*, vol. 28, no. 10, pp. 1477–1500, 2002. [Online]. Available: https://www.sciencedirect.com/science/article/pii/S0167819102001515

[30] D. Krige, ""a statistical approach to some mine valuation and allied problems on the witwatersrand"," Ph.D. dissertation, University of the Witwatersrand, 1951.

[31] X. Lu, J. Huang, L. Song, and J. Li, "An improved geometric parame-

ter airfoil parameterization method," *Aerospace Science and Technology*, vol. 78, pp. 241–247, 2018.

국문 초록

직접수치해석을 이용한 화성 탐사 헬기용 익형 최적 설계 및 로터 공력 성능 분석

박성중
서울대학교 대학원
항공우주공학과

본 연구에서는 화성 대기의 낮은 레이놀즈 수 환경에 맞춘 직접 수치 시뮬레이션(DNS) 기반의 에어포일 설계 최적화 및 3차원 로터 공력 해석을 제시한다. 피트 크레이터 탐사 중 Mars Airborne Explorer(MAE)의 호버 성능을 향상시키기 위해, 블레이드의 세 개 반경 위치에서 에어포일을 최적화하여 설계 양력 계수 범위 전반에서 평균 항력을 최소화하였다. 최적화에는 비균일 유리화 B-스플라인(NURBS)을 사용한 개선된 형상 매개변수화(IGP) 기법과 대리모델 기반의 효율적인 전역 최적화가 적용되어 설계 공간을 효율적으로 탐색하였다. 최적화된 에어포일은 기준 에어포일인 clf5605에 비해 평균 항력이 21–28% 감소함을 보여주었다. 이러한 성능 향상은 주로 Sharp Raised-Lip(SRL) 및 얇은 캠버 형상을 통해 이루어지며, 이는 전연 전단층 분리를 유도하고 피부 마찰 항력을 줄인다. 최적화된 에어포일은 전체 3차원 로터에 통합되어 호버 조건에서 평가되었다. 결과적으로 설계 추력 조건에서 Figure of Merit(FM)이 7% 증가하고 동력 계수

는 7.6% 감소하였다. 최적화된 에어포일의 2차원 및 3차원 특성을 비교한 결과, 블레이드 중간부에서는 두 환경 모두에서 유사한 특성을 보였으나, 외측 팁 영역에서는 스팬 방향 유동으로 인해 비정상성이 유발되어 거동 차이가 나타났다. 또한, 로터의 넓은 추력 범위에서 성능 변화를 조사하기 위해 오프 디자인 해석도 수행되었다.

주요어: 익형 최적설계, 화성 헬리콥터, 3차원 로터 공력해석, 저 레이놀즈 수, 직접 수치 해석

학번: 2023-28011